計測情報処理論
「太陽系探査データ処理」
Analysis of solar system exploration data

新領域創成科学研究科　複雑理工学専攻
今村 剛　Takeshi Imamura

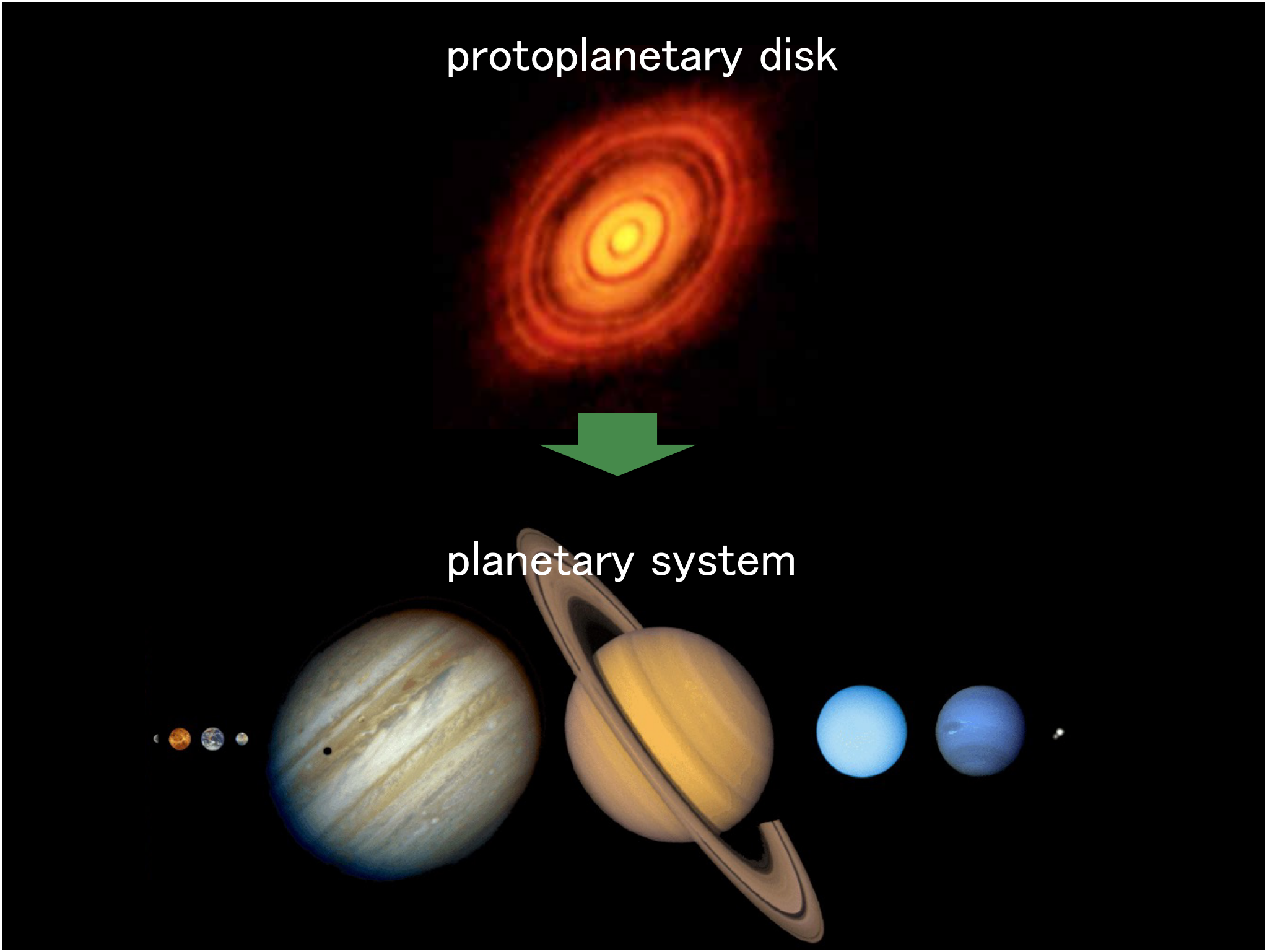
protoplanetary disk
planetary system

Observation methods

Pros and Cons

	Lander	Orbiter	Ground-based observation
Spatial coverage	Limited	Global	Global
Time coverage	Short in many cases	Long, continuous	Repeatable
Observable variables	- Direct sampling - Chemical analysis	- Radio/optical remote sensing - In-situ plasma measurements	- Optical/radio remote sensing - Instruments can be large

Recent remote-sensing orbiter missions

Venus Express

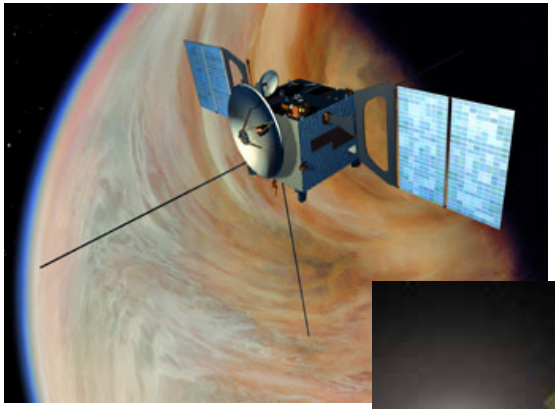

Akatsuki

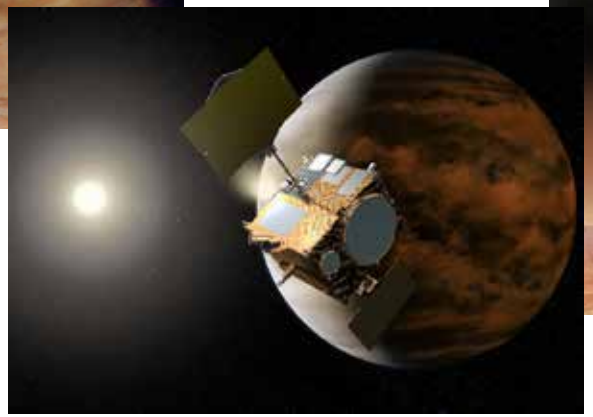

Mars Reconnaissance Orbiter

JUNO

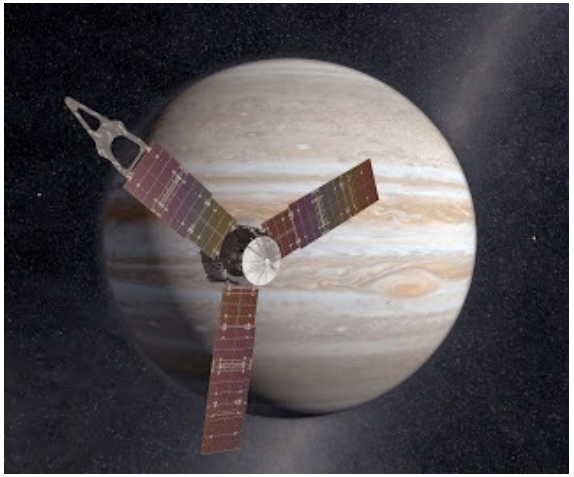

MMX

ExoMars Trace Gas Orbiter

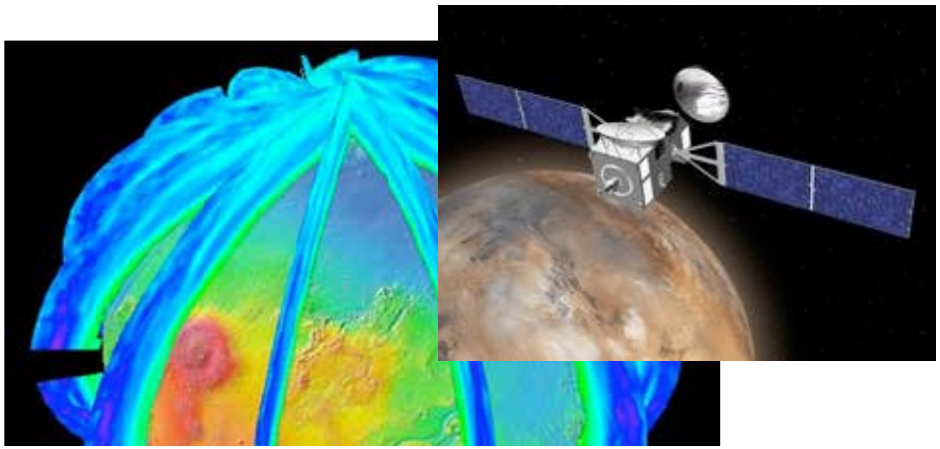

JUICE

Remote sensing in planetary exploration

- Radio wave measurement
  - Doppler measurement of spacecraft signals
  - Spectroscopy
  - Radar
  - Radio interferometry (e.g, VLBI)
- Optical (short wavelength EM wave) measurement
  - Imagery
  - Spectroscopy
  - Laser sounding

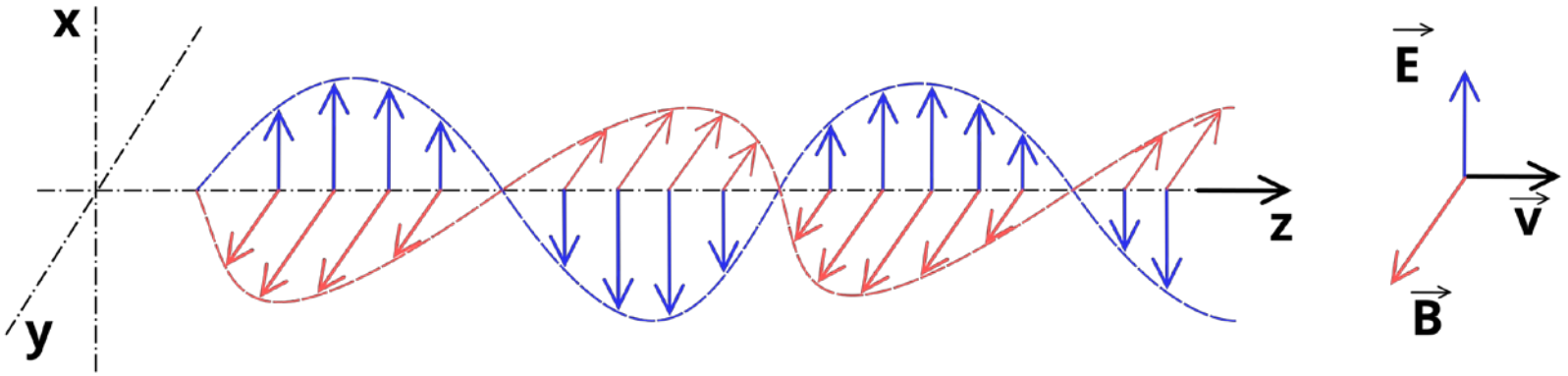

from Wikipedia

Vertical temperature profiles of planetary atmospheres

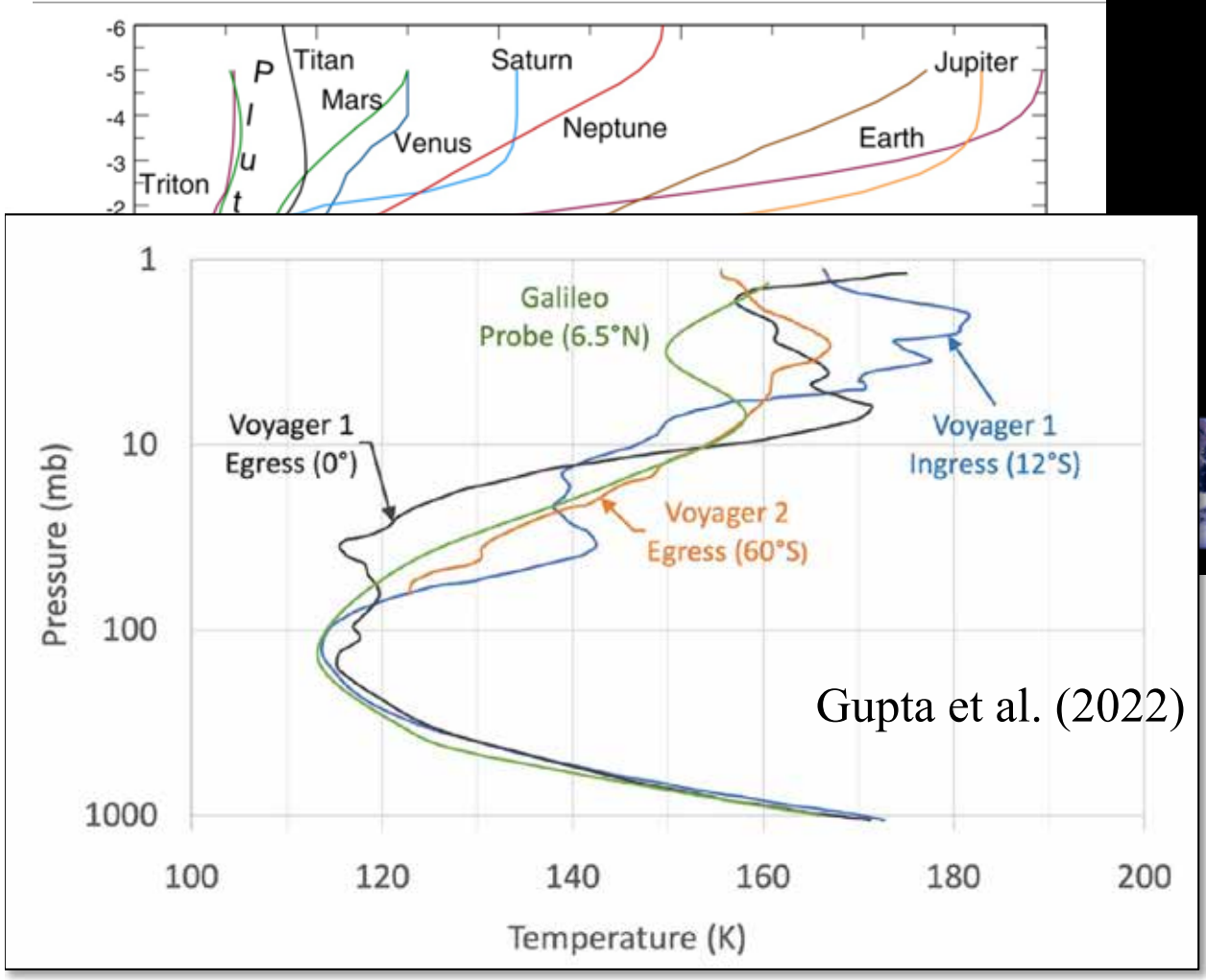

Gupta et al. (2022)

Radio occultation observation of planetary atmosphere

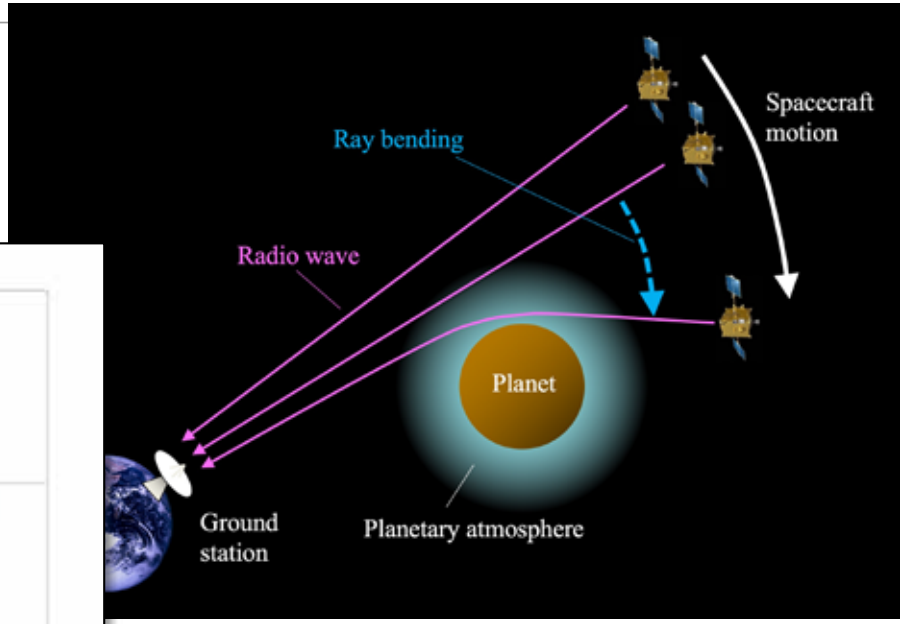

Radio occultation measurement

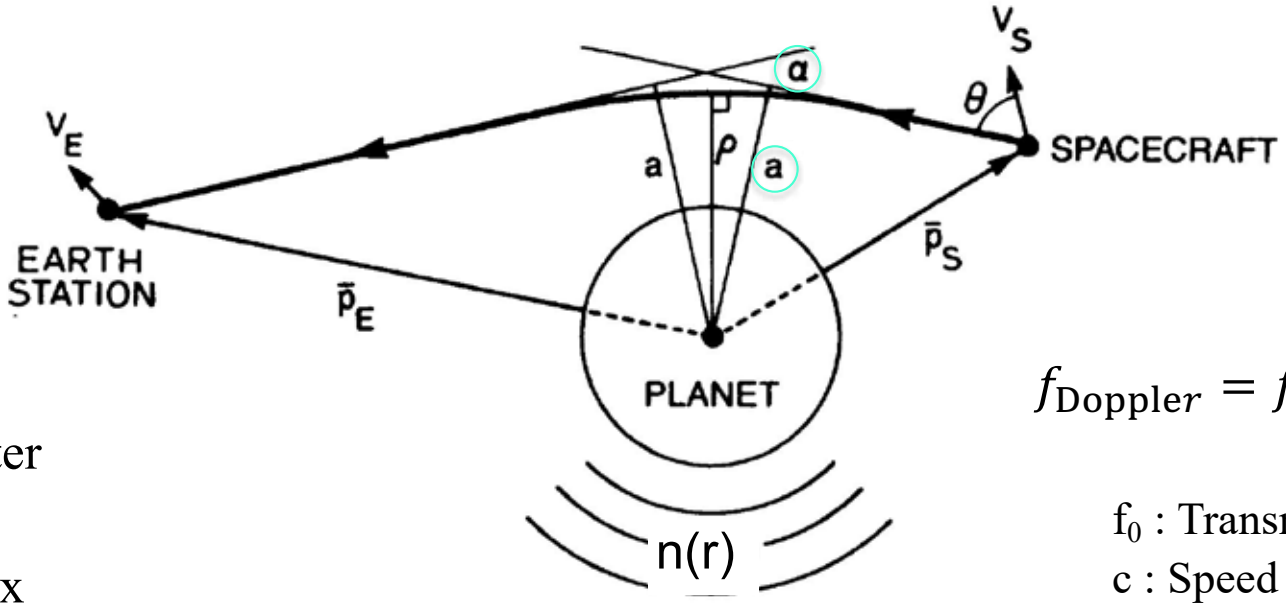

Tyler (1987)

$$f_{\mathrm{Doppler}} = f_0 \frac{V_S \cos\theta}{c}$$

a : Impact parameter
α : Bending angle
n : Refractive index
r : Distance from planet center

f_0 : Transmit frequency
c : Speed of light

Abel transformation to obtain the refractive index profile

$$\ln n(r) = -\frac{1}{\pi}\int_{a_1}^{\infty} \ln\left\{\frac{a}{a_1} + \left[\left(\frac{a}{a_1}\right)^2 - 1\right]^{\frac{1}{2}}\right\} \frac{d\alpha}{da} da$$

$n(r)\, r = a$ a : Impact parameter for a ray whose radius of closest approach is r

Refractive index n is related to atmospheric structure:

$$\mu(r) = (n(r) - 1) \times 10^6$$

$$= \kappa N_n(r) - 40.3 \frac{N_e(r)}{f_0^2} \times 10^6$$

neutral atmosphere

plasma

μ : Refractivity

N_n : Neutral number density

N_e : Electron number density

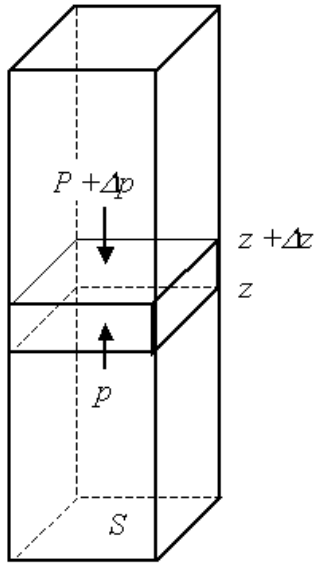

Neutral atmosphere's temperature based on hydrostatic equilibrium:

$$T(r) = \frac{N_n(r_{top})}{N_n(r)} T(r_{top}) + \frac{\overline{m}}{k N_n(r)} \int_r^{r_{top}} N_n(r') g(r') dr$$

$$-S\Delta p = g\rho S\Delta z$$

$$\therefore \frac{dp}{dz} = -g\rho$$

$$p(z) = \int_z^{\infty} g\rho(z')dz'$$

(Temperature at the upper boundary should be given from empirical models. The effect of the upper boundary almost disappears 1-2 scale heights below the boundary)

Retrieval of a temperature profile

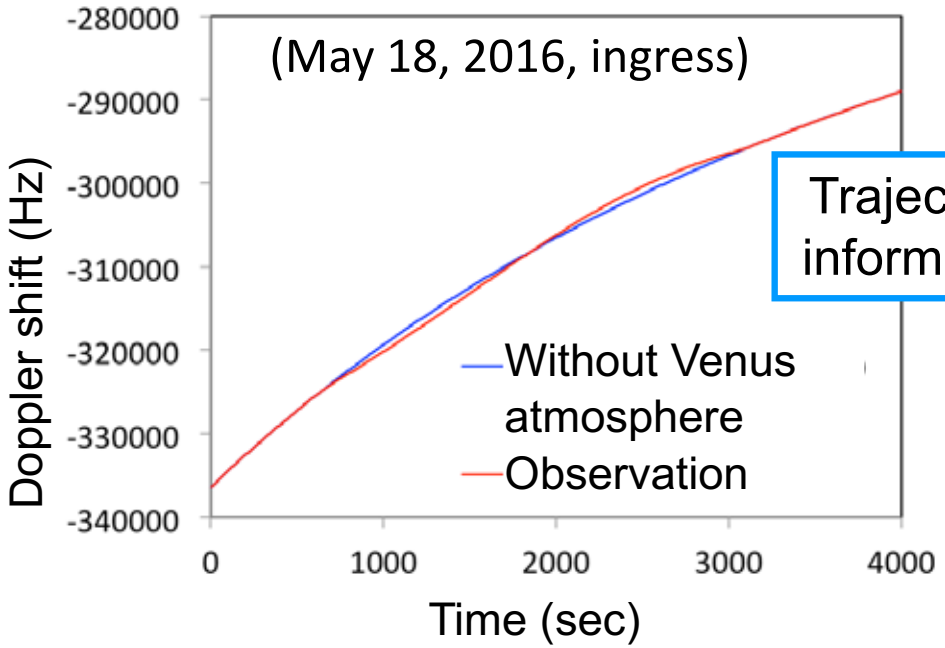

Trajectory information

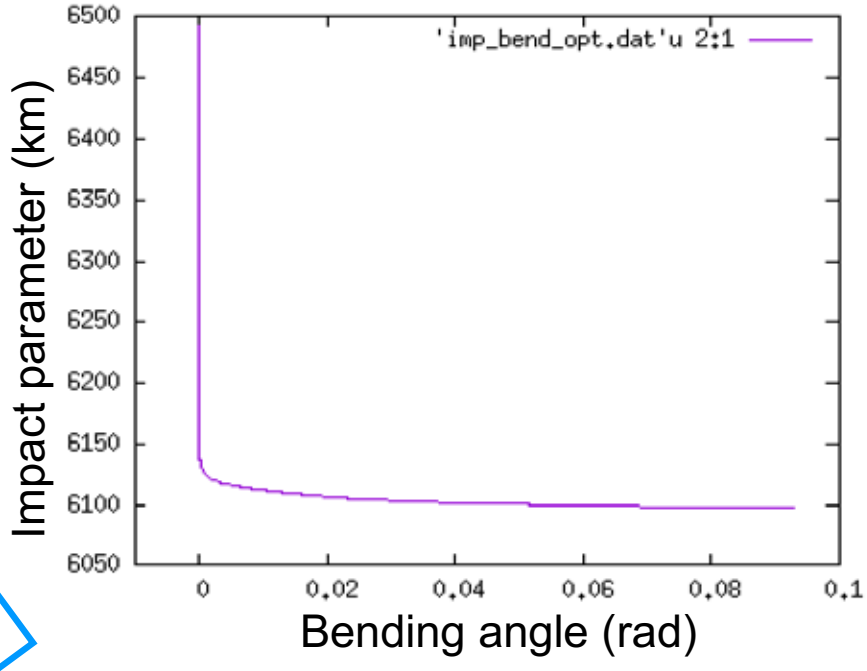

Abel transform

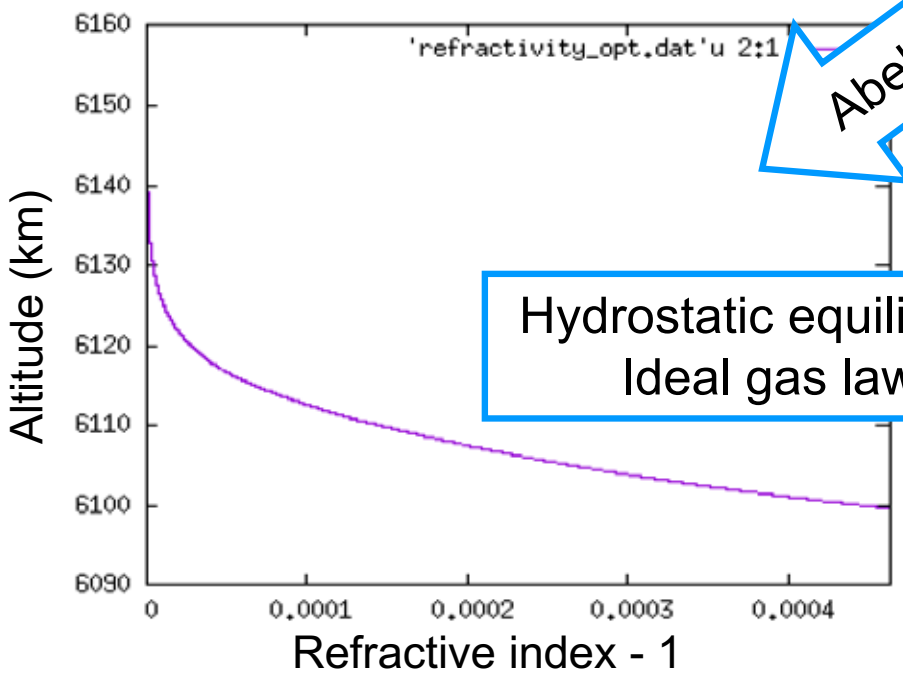

Hydrostatic equilibrium
Ideal gas law

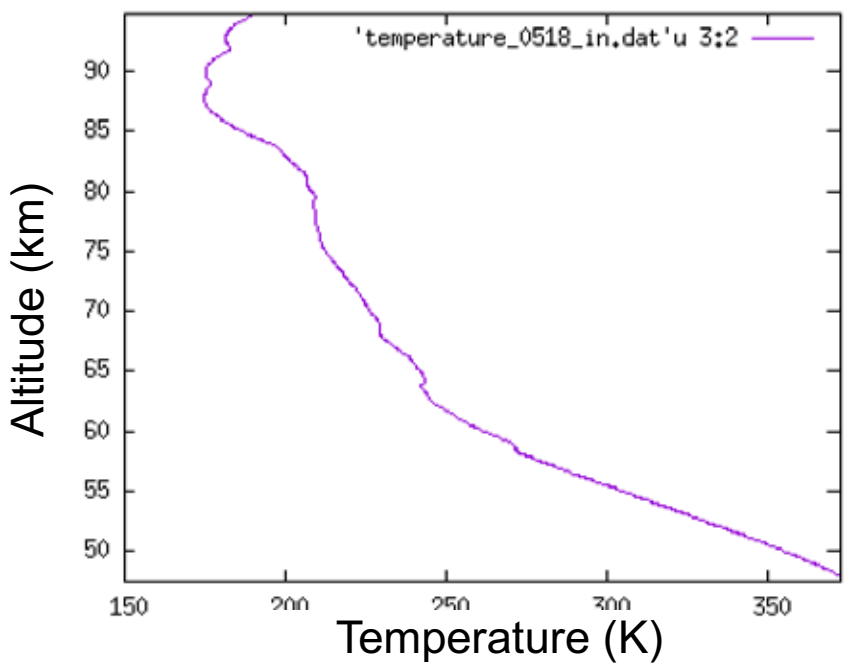

Frequency stability of the radio source: Allan deviation

Allan variance

$$\sigma_y^2(\tau) = \frac{1}{2}\left\langle (\bar{y}_{n+1} - \bar{y}_n)^2 \right\rangle$$

$$\bar{y}_n = \frac{f_n}{f_0}$$: n-th fractional frequency average over the observation time τ

(f_n : n-th measurement of frequency

f_0 : Nominal frequency)

Allan deviation

$$\sigma_y(\tau) = \sqrt{\sigma_y^2(\tau)}$$

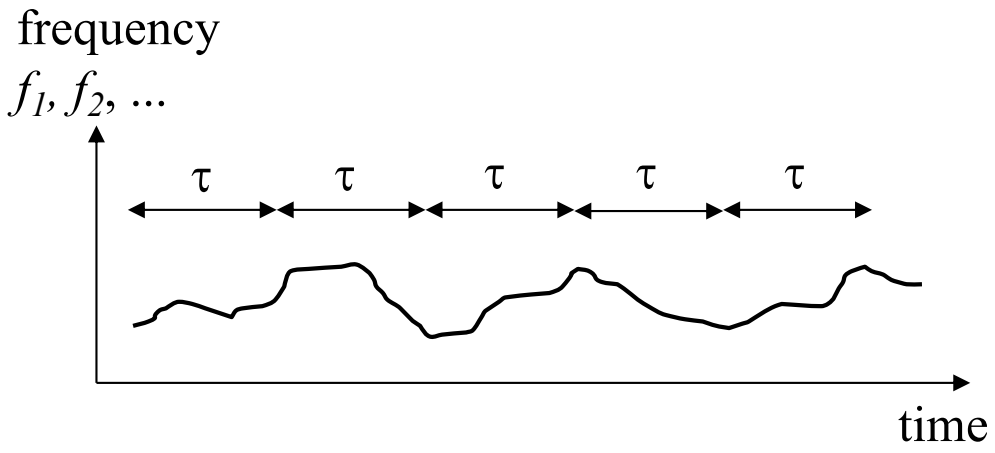

Ultra-Stable Oscillator (USO) on Venus orbiter Akatsuki

Frequency stability of the USO

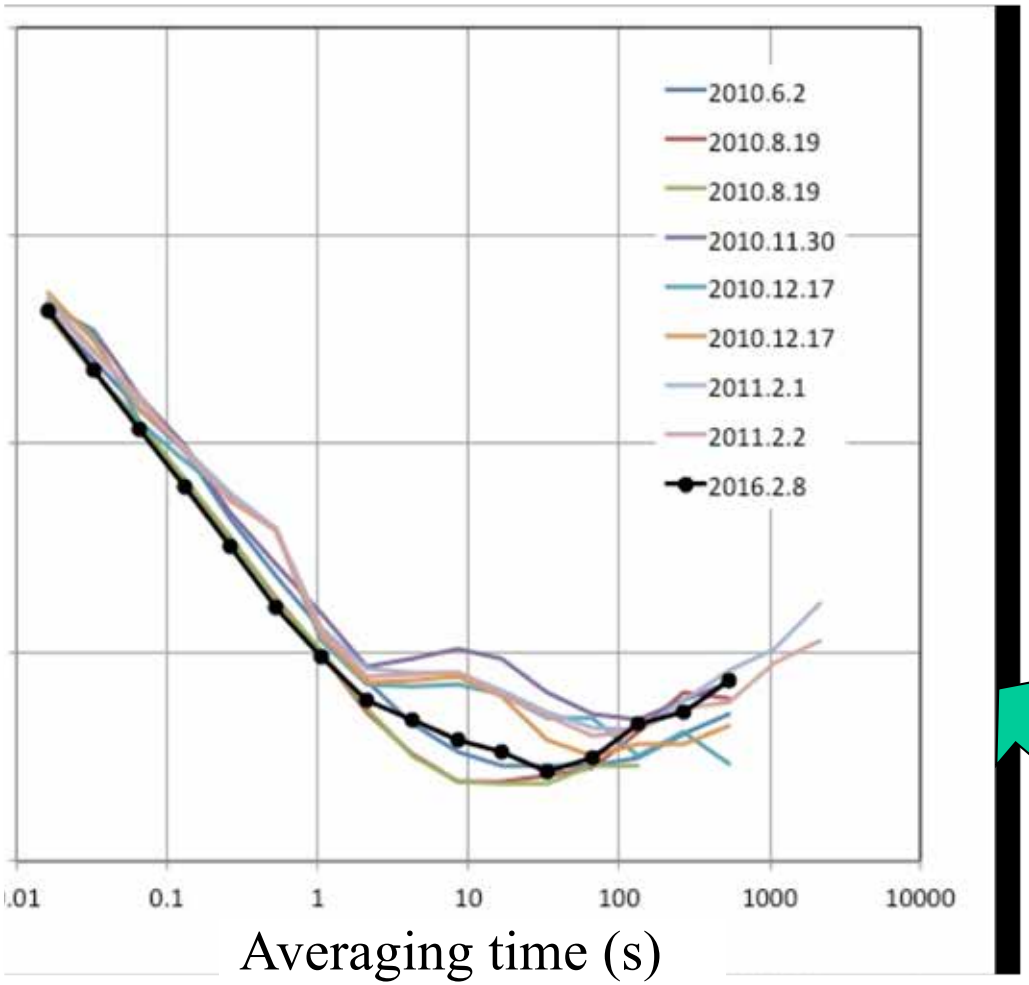

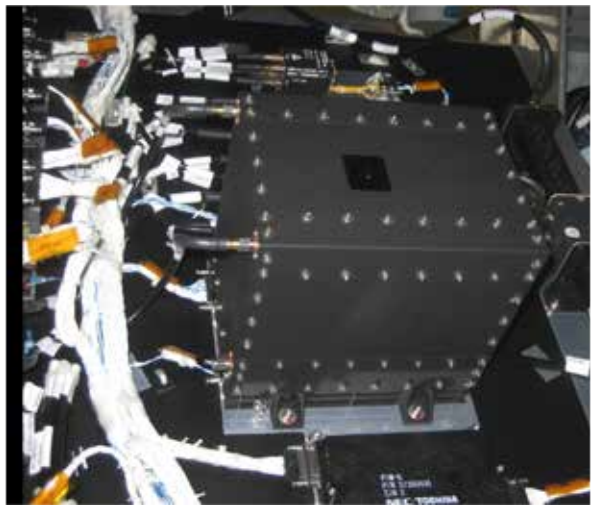

USO on Akatsuki

Frequency stabilities of quartz oscillators for commercial use are typically ~10^{-8}

Data acquisition

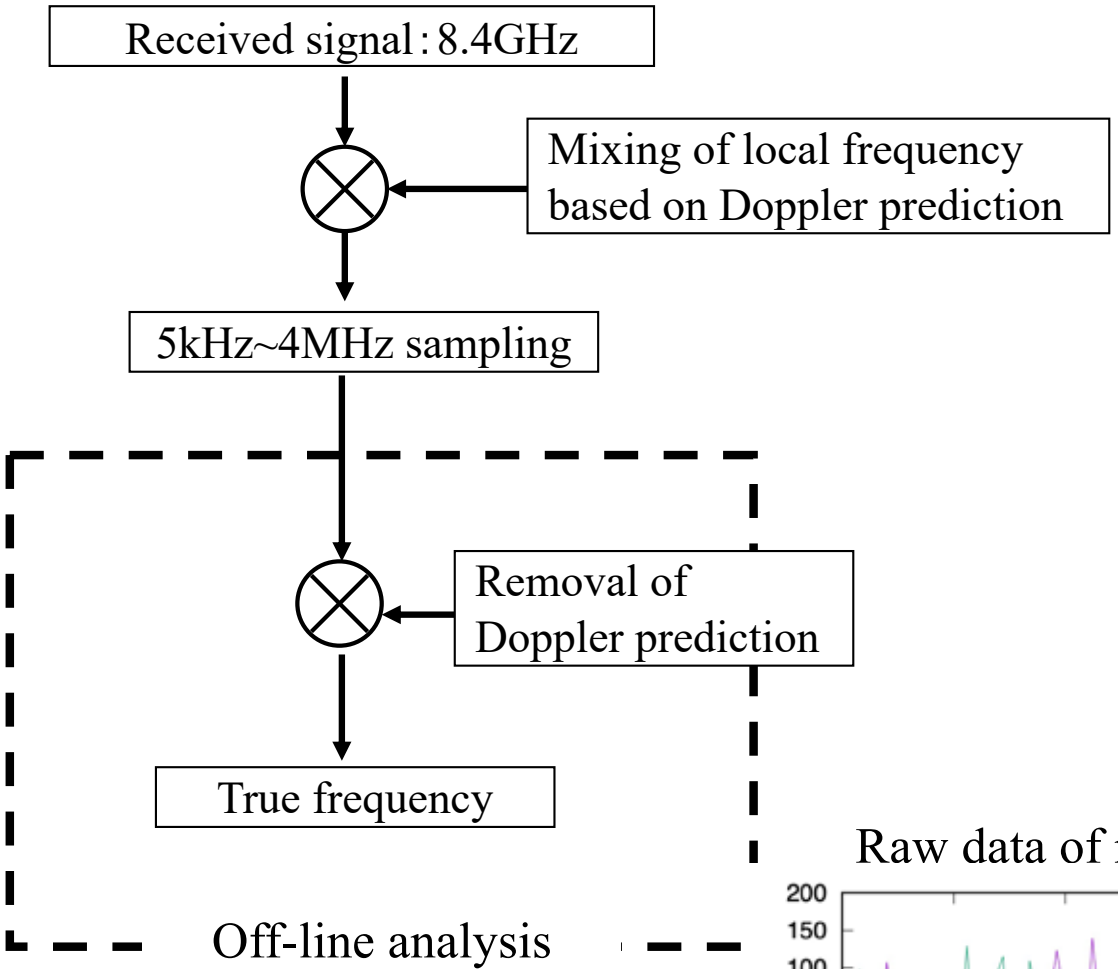

Usuda Deep Space Center (UDSC)

Raw data of radio wave from Venus orbiter Akatsuki

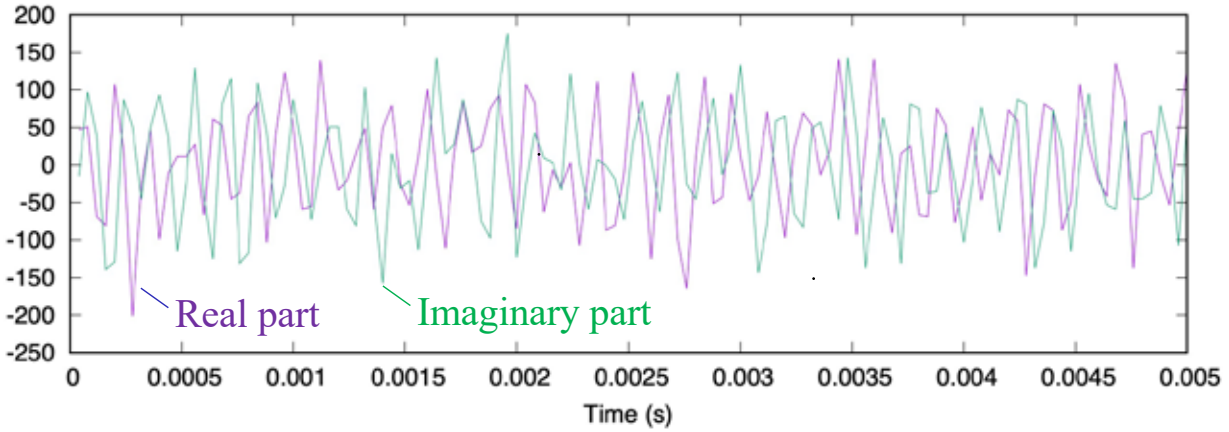

Rough estimation of frequency

Successive FFTs for short segments

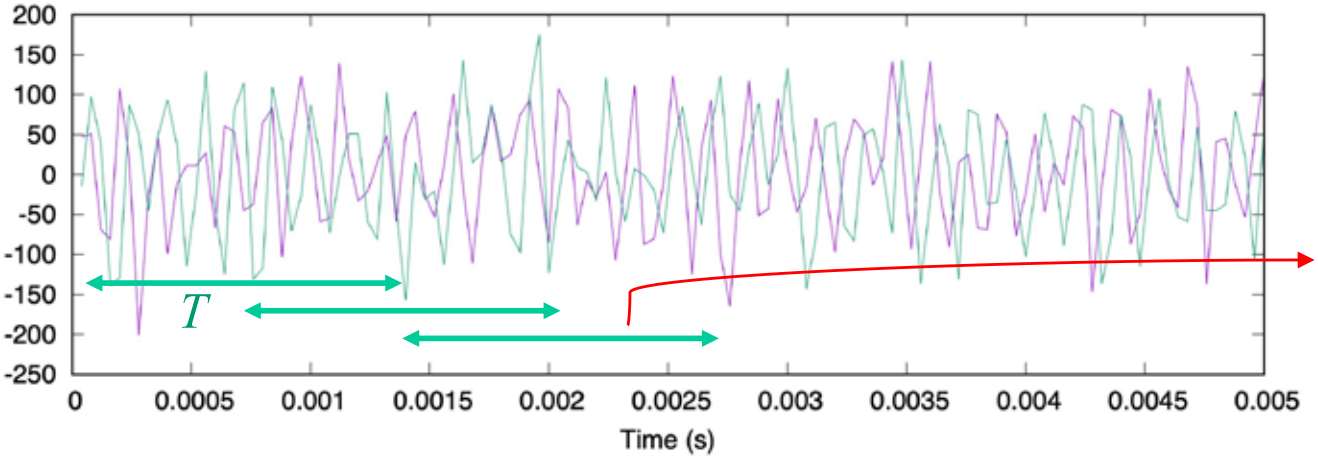

Fitting of Sinc function

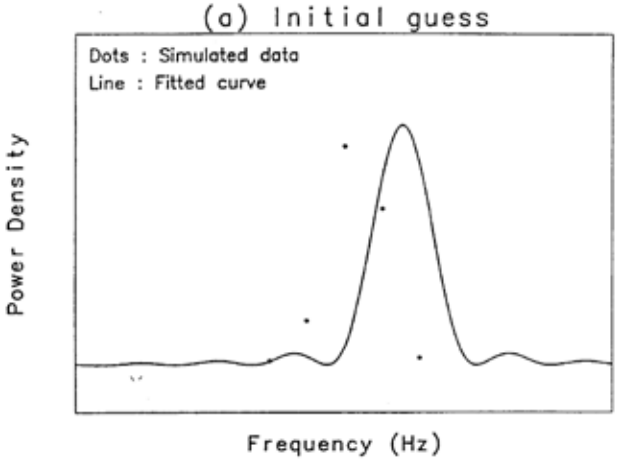

Frequency resolution of FFT

$$\Delta f = 1/T$$
$$= B/N$$

T : Time length of FFT
N : FFT length
B : Bandwidth = sampling frequency (for complex data)

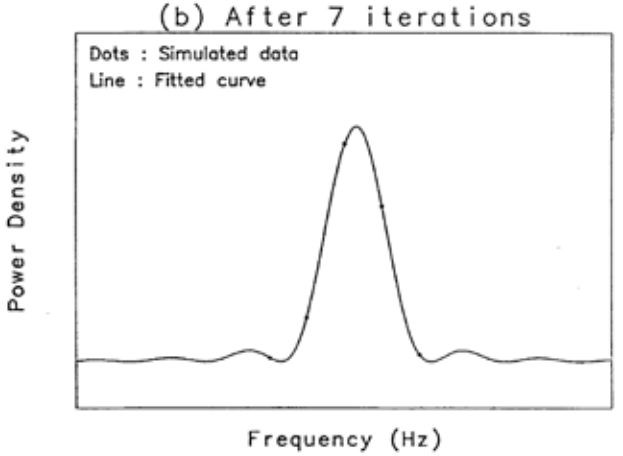

For example, to achieve a frequency accuracy of $\Delta f < 0.1$ Hz, the time length should be $T = 1/\Delta f > 10$ s.

Rough estimation of frequency

Successive FFTs for short segments

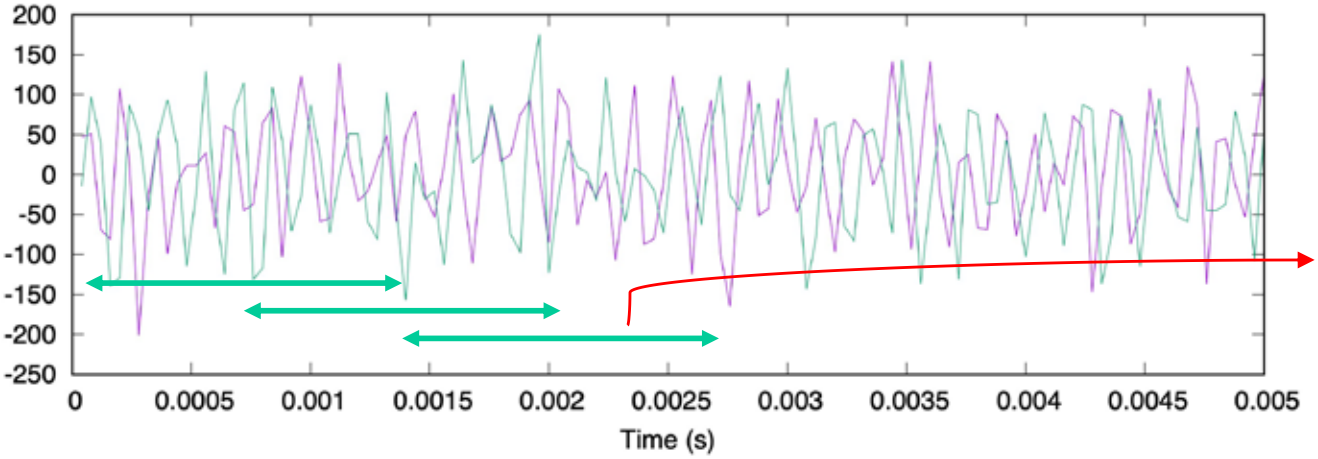

Fitting of Sinc function

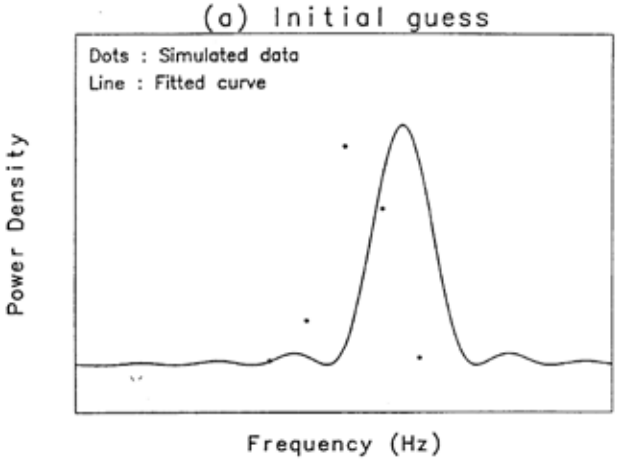

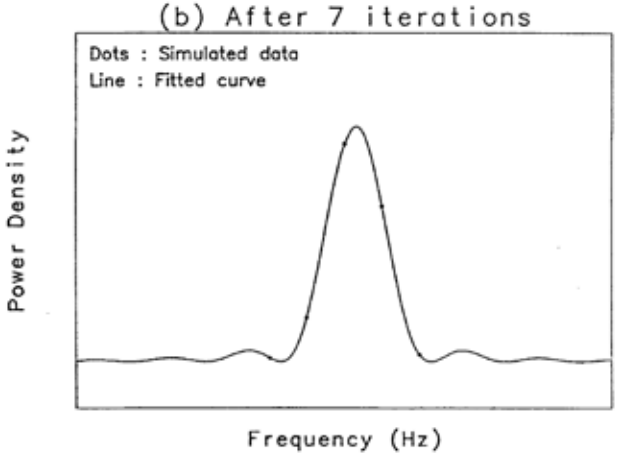

Rough estimate of the frequency time series

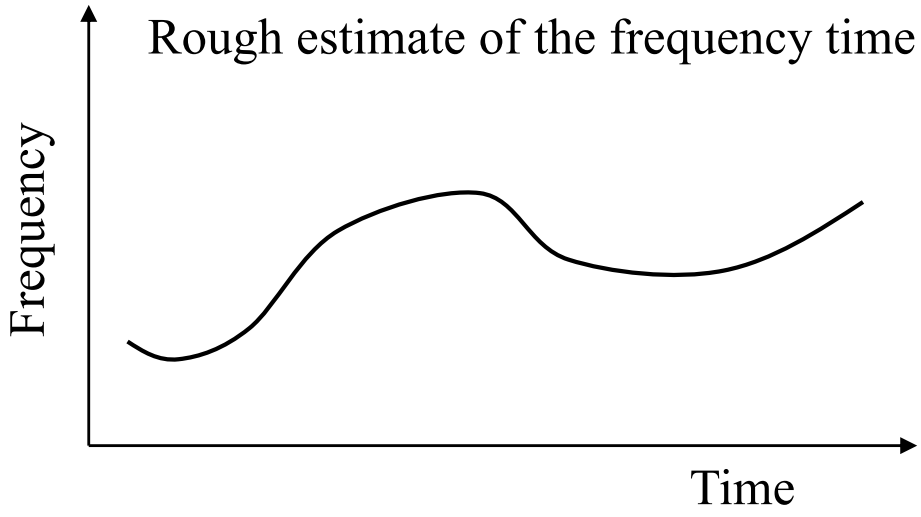

Subtraction of the roughly estimated frequency to obtain the precise phase

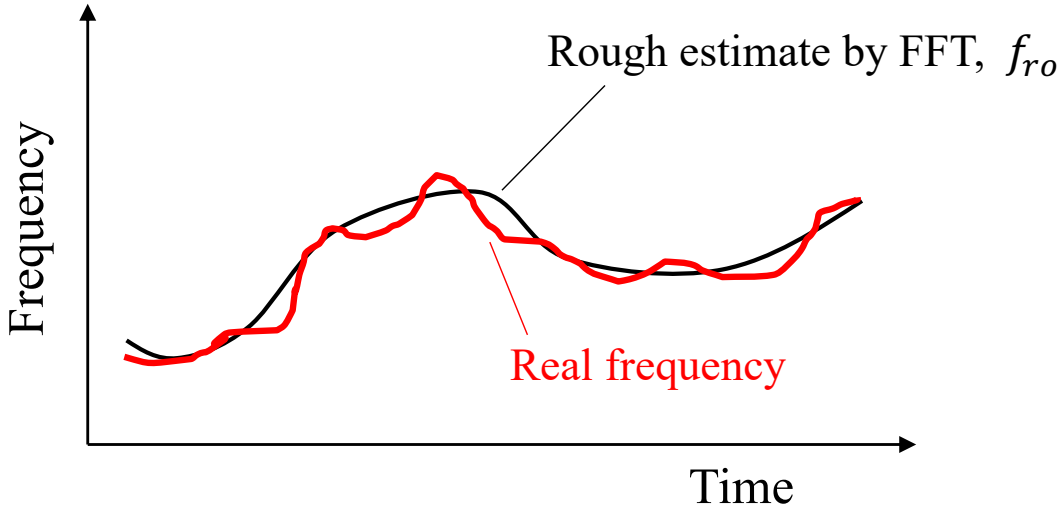

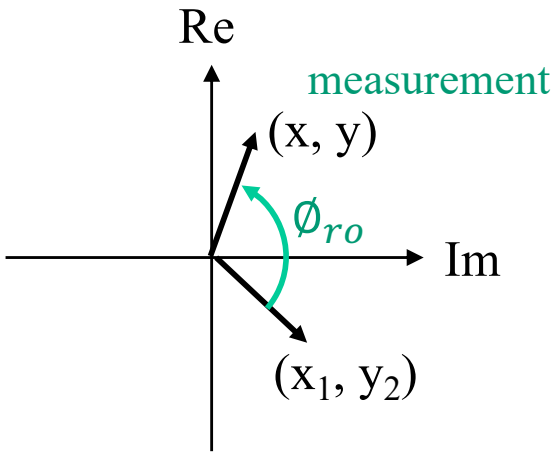

phase correction

$$\emptyset_{ro}(t) = \int^{t} f_{ro}(t')dt'$$

$$\begin{pmatrix} x_1(t) \\ y_2(t) \end{pmatrix} = \begin{pmatrix} \cos(-\emptyset_{ro}) & -\sin(-\emptyset_{ro}) \\ \sin(-\emptyset_{ro}) & \cos(-\emptyset_{ro}) \end{pmatrix} \begin{pmatrix} x(t) \\ y(t) \end{pmatrix}$$

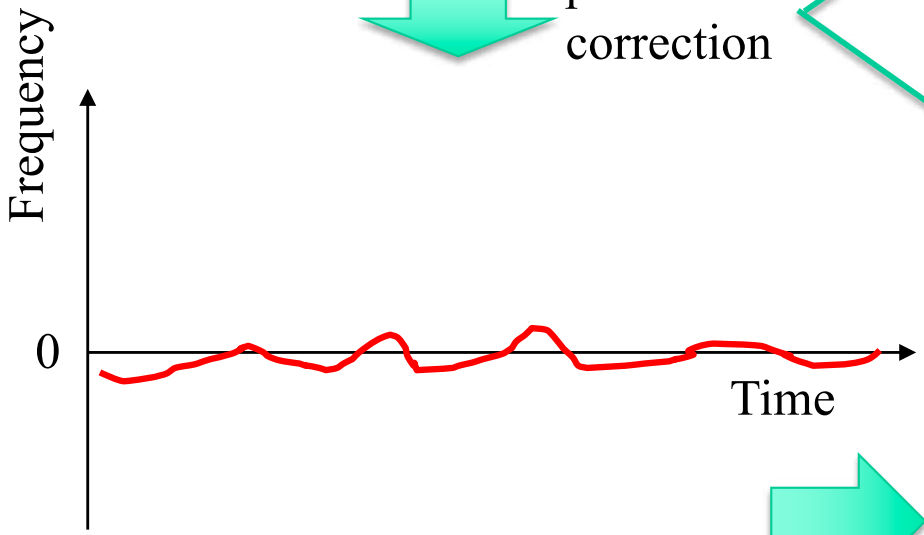

Narrow-band filtering

Filtering and decimation

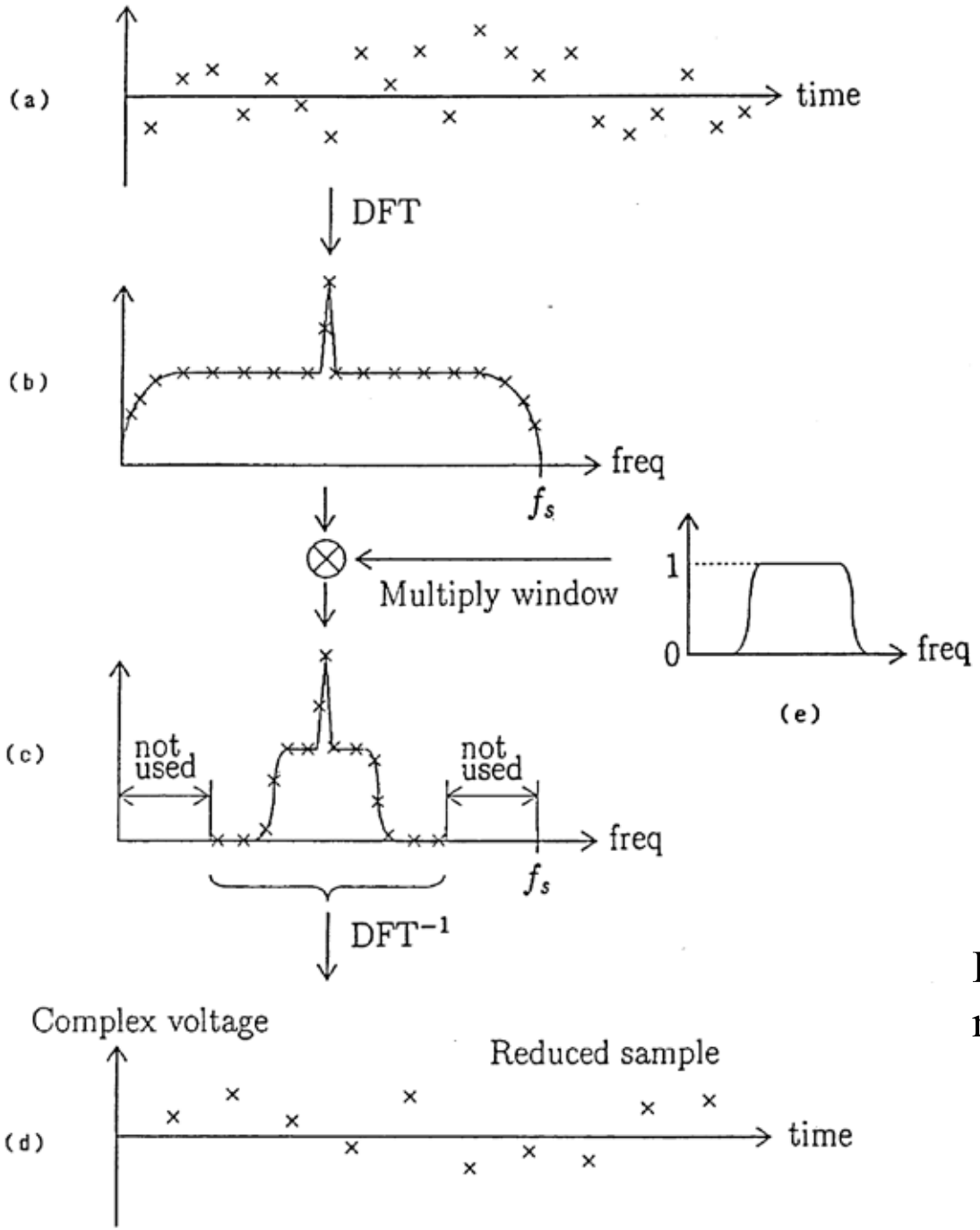

Low-noise data is created by narrow-band filtering

Precise phase/frequency estimation by phase unwrapping

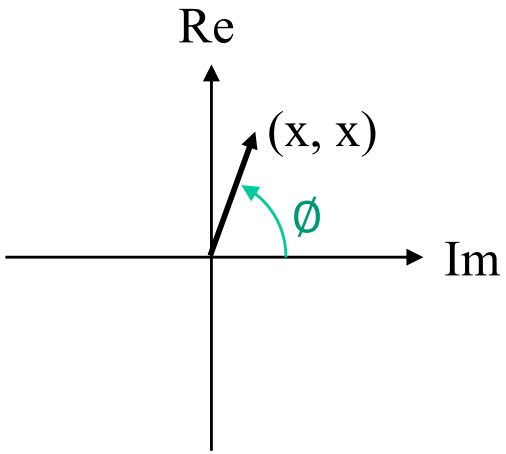

Frequency

$$f = \frac{d\emptyset}{dt}$$

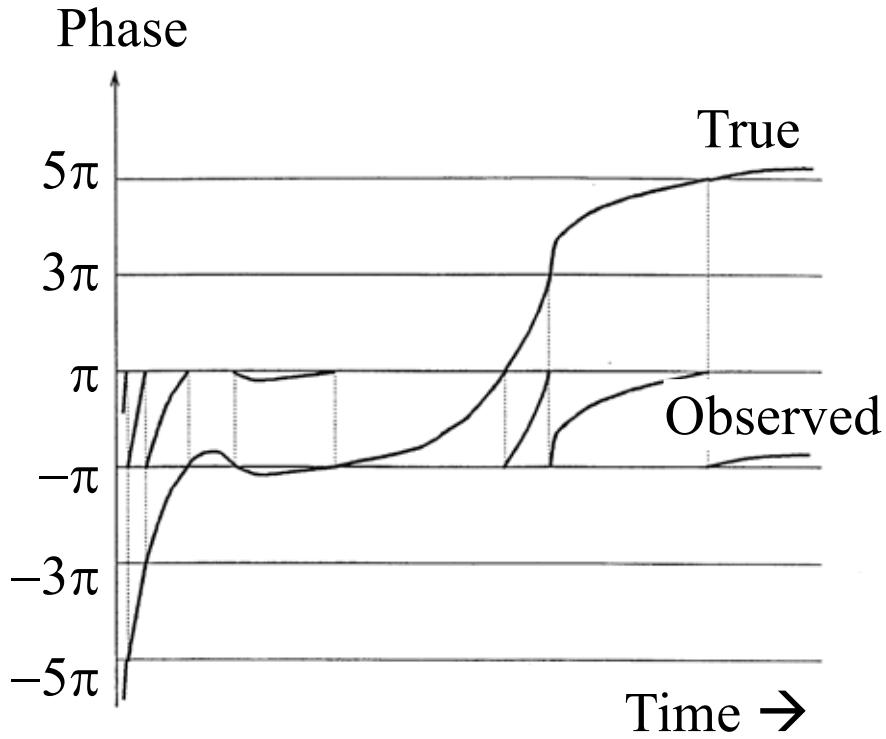

With sufficiently low-noise, the phase can be obtained from the real and imaginary components of the data at each time step. The frequency is obtained by differentiating the phase.

Temperature profiles of the Venus atmosphere obtained by Akatsuki radio occultation

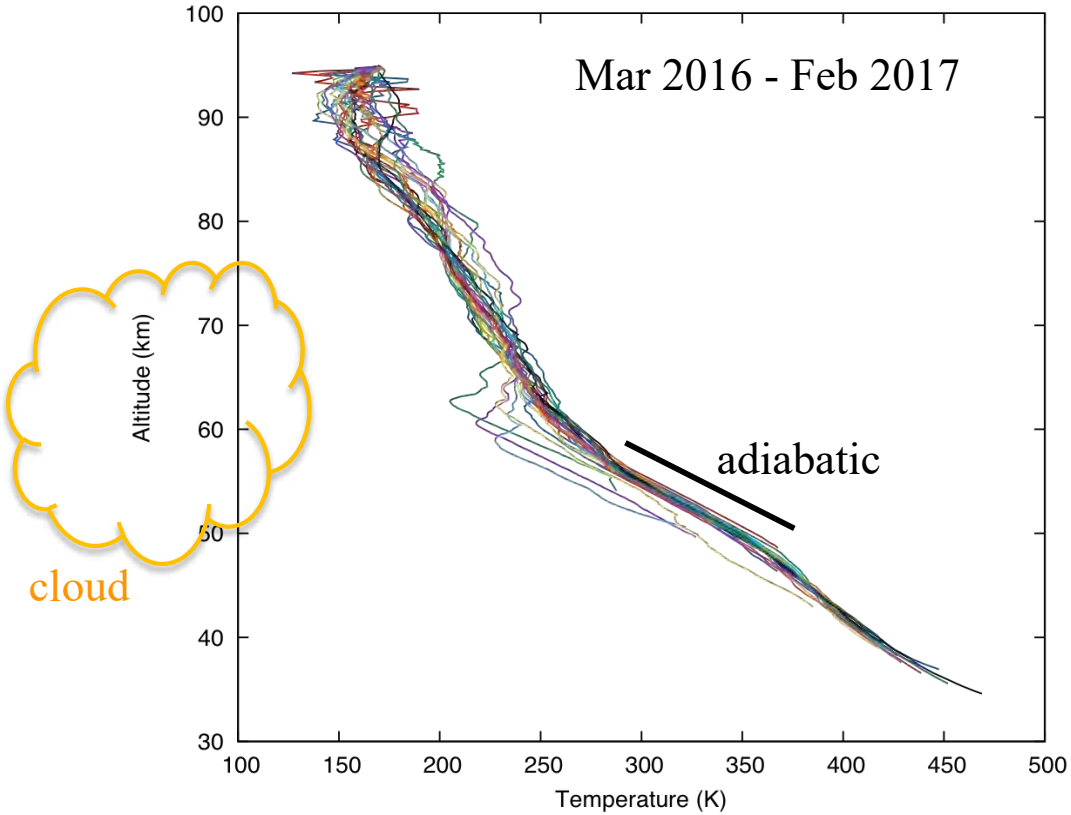

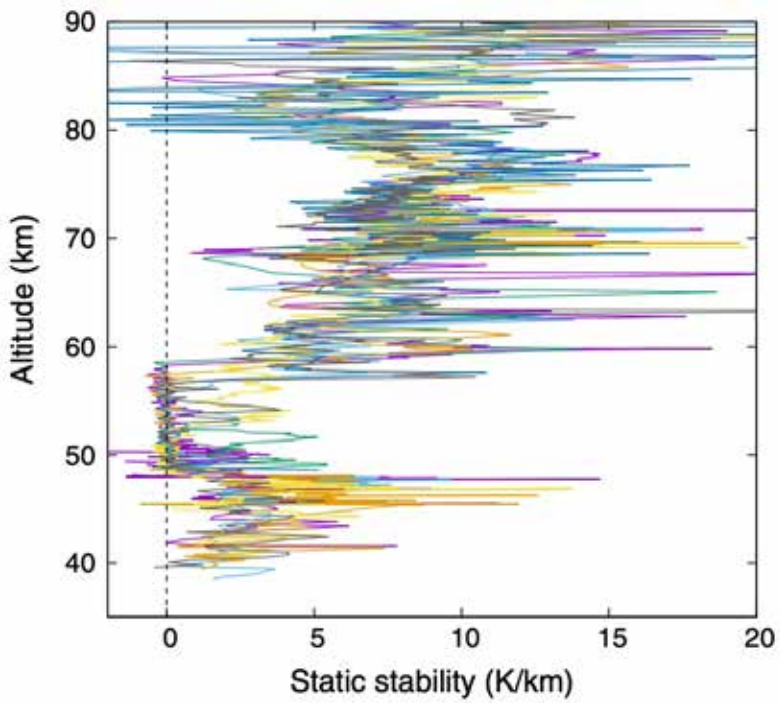

Imamura et al. 2017

Static stability: $$S = \frac{dT}{dz} - \frac{g}{c_p}$$

T : temperature
z : altitude
g : gravitational acceleration
c_p : specific heat for constant pressure

Latitude-altitude cross sections

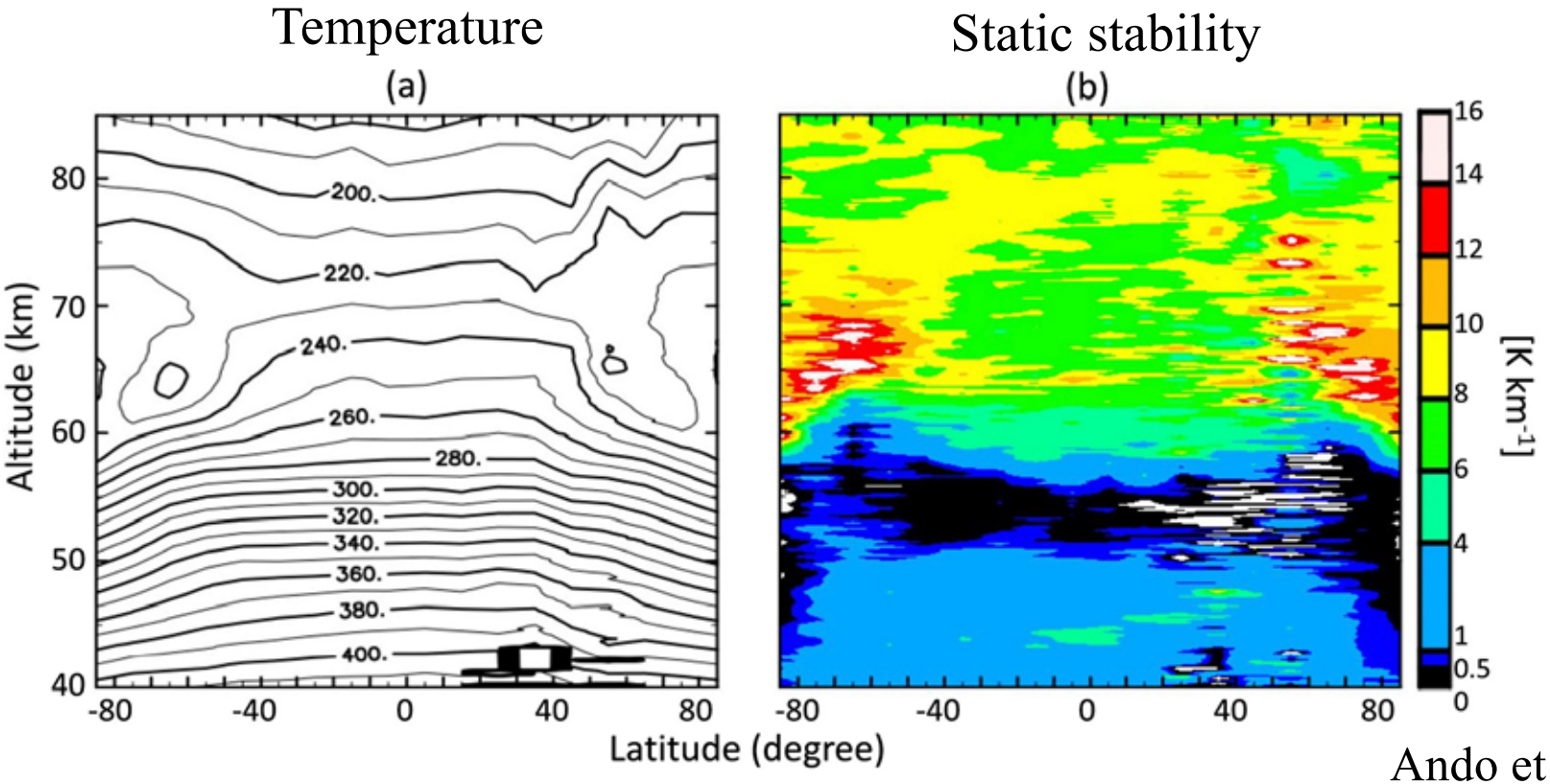

Ando et al. (2020)

Figure 2. Latitude–height distributions of zonally and temporally averaged (**a**) temperatures and (**b**) static stability obtained from Venus Express and Akatsuki radio occultation measurements.

- Near-neutral layer extends to the sub-cloud region in the high latitude
- Unknow energy transport below clouds ?

Examples of Venus' electron density profile (from Akatsuki radio occultation)

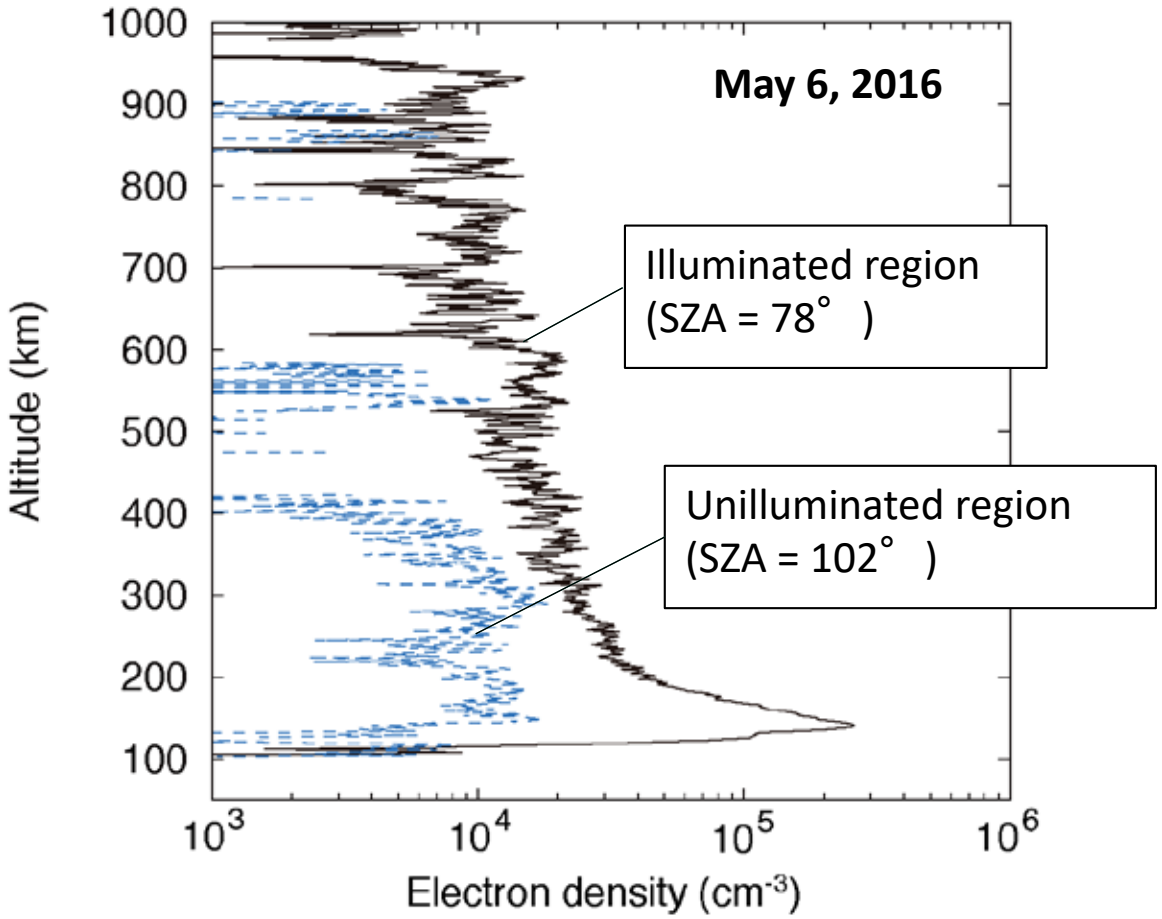

$$\mu(r) = (n(r) - 1) \times 10^6$$

$$= \kappa N_n(r) - 40.3 \frac{N_e(r)}{f_0^2} \times 10^6$$

neutral atmosphere

plasma

μ : Refractivity

N_n : Neutral number density

N_e : Electron number density

Radio occultation of lunar photoelectron layer with SELENE

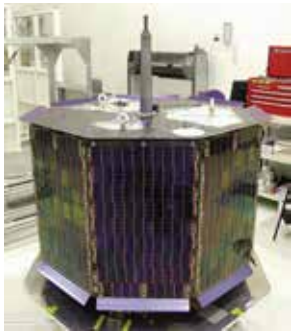

Vstar subsatellite

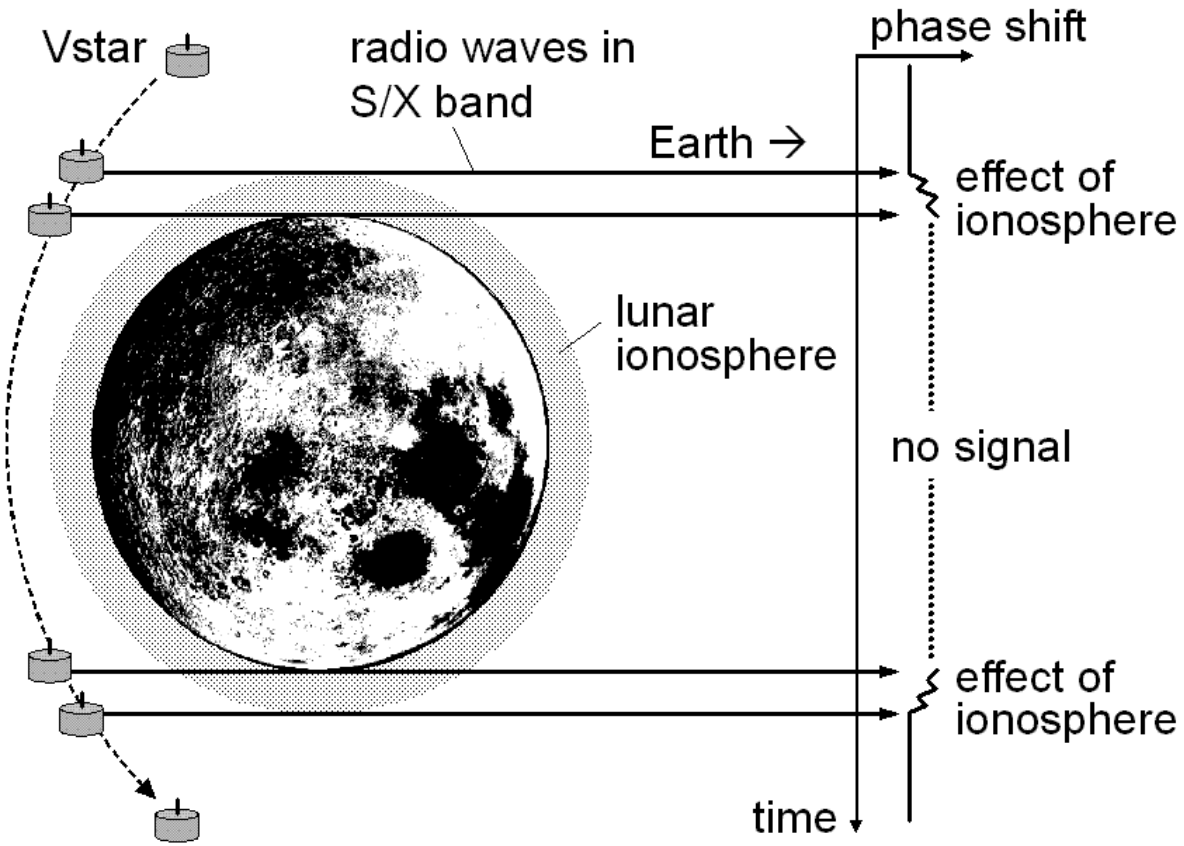

Usuda Deep Space Center, Japan

Dual-frequency method for plasma measurement

To remove the effect of the fluctuation of the transmitted signal's frequency and the neutral atmosphere's contribution, two frequencies generated from the common onboard oscillator are used. A linear combination of these phases can extract the plasma contribution.

$$\Delta\phi_S = -\frac{40.3}{c f_S} N_e + \alpha f_S$$: Phase shift of S-band (2.3 GHz)

$$\Delta\phi_X = -\frac{40.3}{c f_X} N_e + \alpha f_X$$: Phase shift of X-band (8.4 GHz)

$$\delta\phi = \Delta\phi_S - \frac{f_S}{f_X}\Delta\phi_X = -\frac{40.3}{c} f_S \left(\frac{1}{f_S^2} - \frac{1}{f_X^2} \right) \cdot N_e$$: Differential phase

N_e : Column electron density
f_S : S-band frequency
f_X : X-band frequency

Example from lunar plasma layer measurement in SELENE mission

Phase deviation in S-band (ϕ_S) and X-band (ϕ_X)

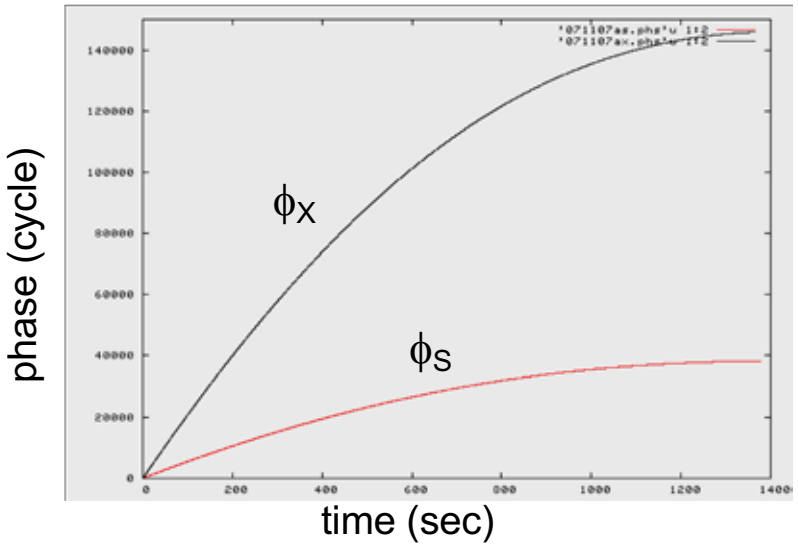

Differential phase $\phi_{diff} = \phi_S - f_s/f_x \, \phi_X$

(f_s, f_x : S/X-band nominal freq.)

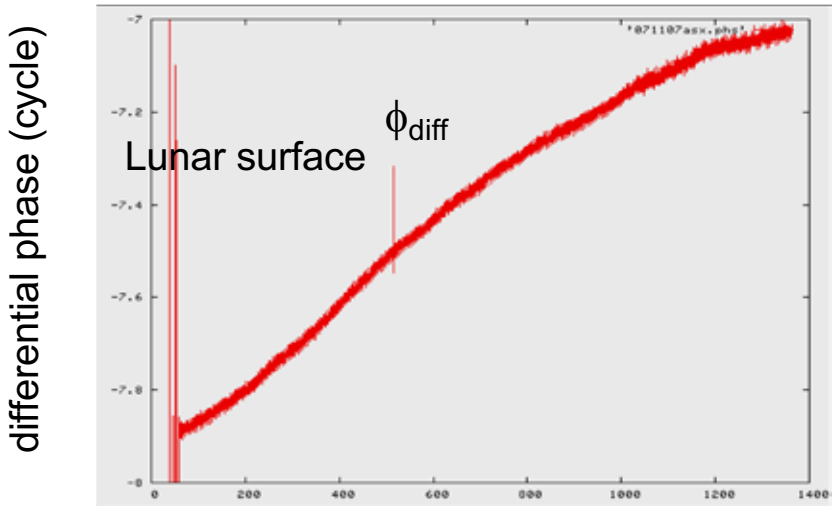

ϕ_{diff} is proportional to the electron density integrated along the ray path.

Mean density profile of lunar ionosphere at SZA<60°

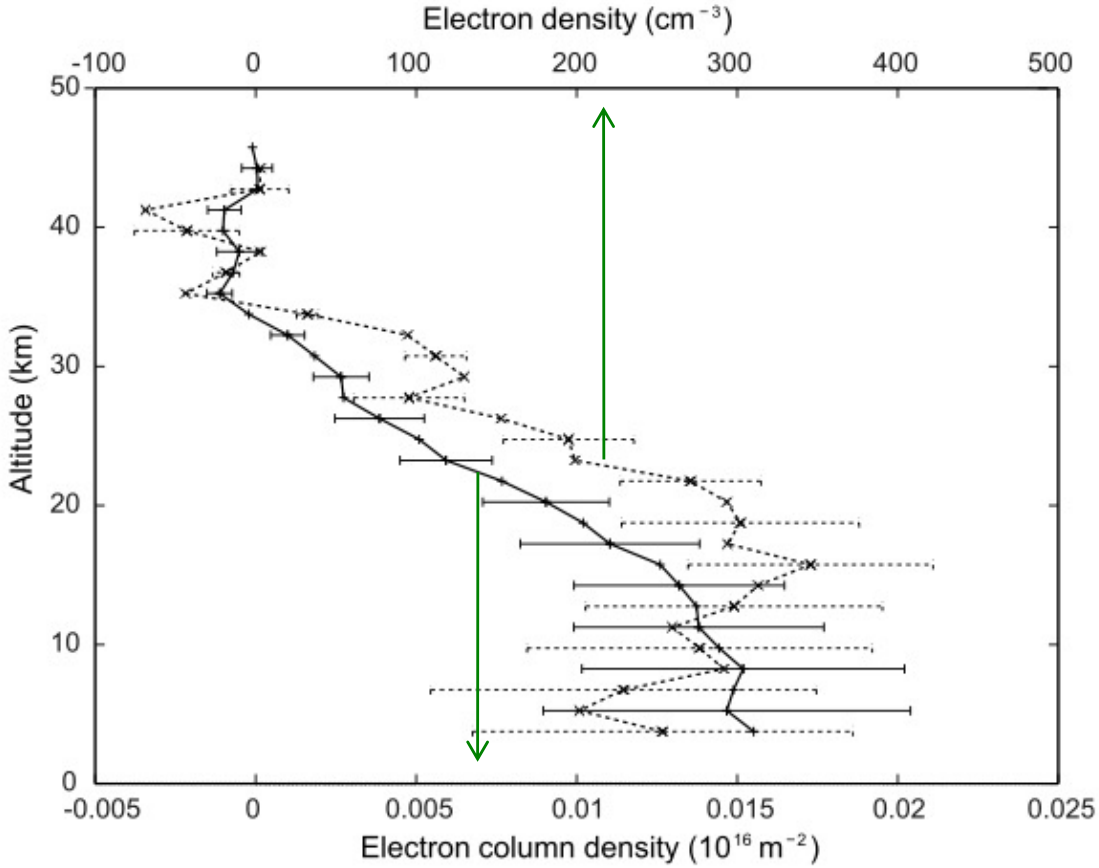

Imamura et al. (2012)

Radio occultation measurements of Pluto's neutral atmosphere with New Horizons

- Pluto has a tenuous atmosphere composed primarily of N_2.
- New Horizons spacecraft performed a radio occultation that sounded Pluto's atmosphere In 2015.
- Signals were transmitted by four ground antennas of the NASA Deep Space Network, and the spacecraft received the signals. The data streams were digitized, filtered, and stored on the spacecraft for later transmission to Earth.

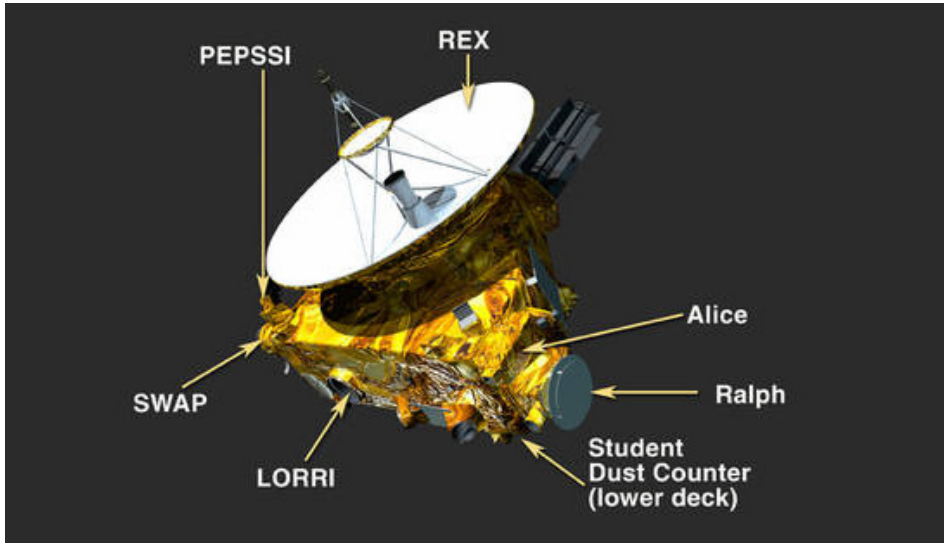

Hinson et al. (2017)

Removal of diffraction effects caused by the surface of Pluto

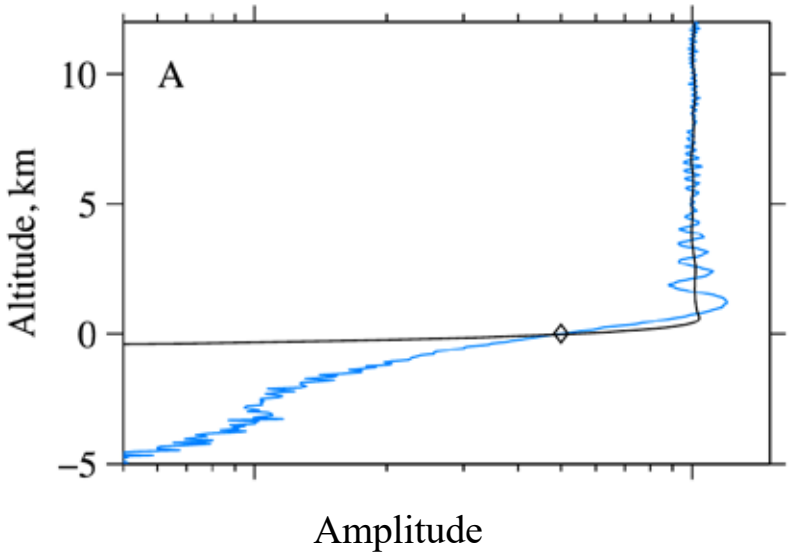

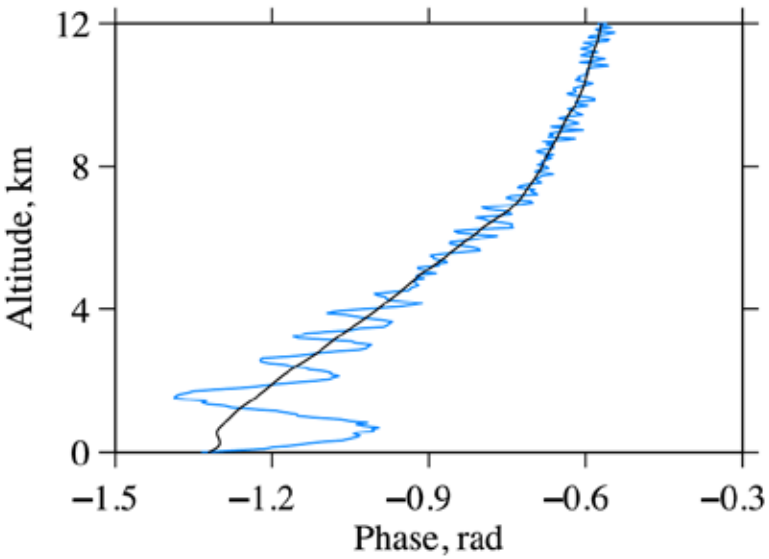

atmospheric profiles

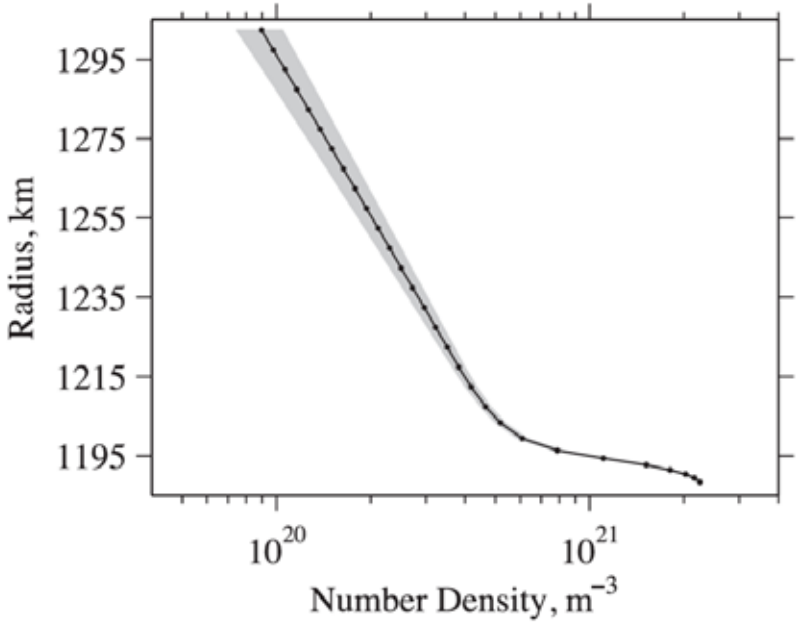

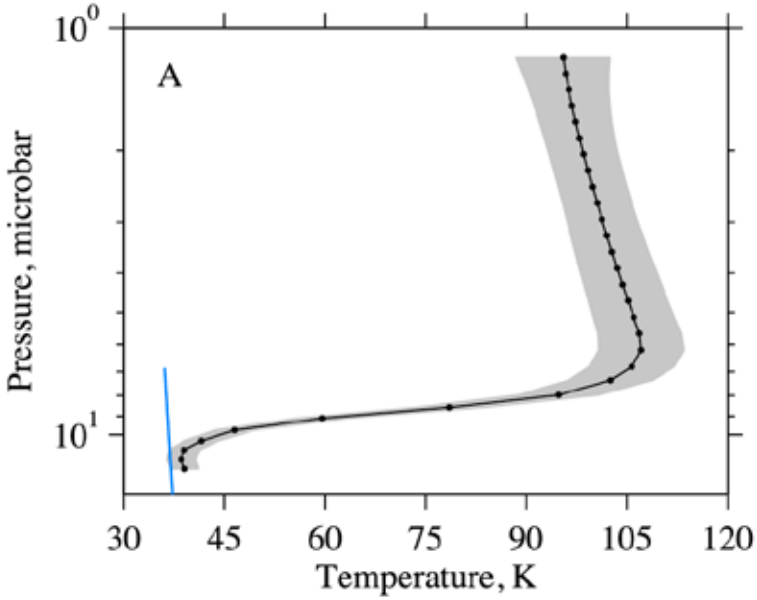

GPS radio occultation for Earth

UCAR/COSMIC homepage

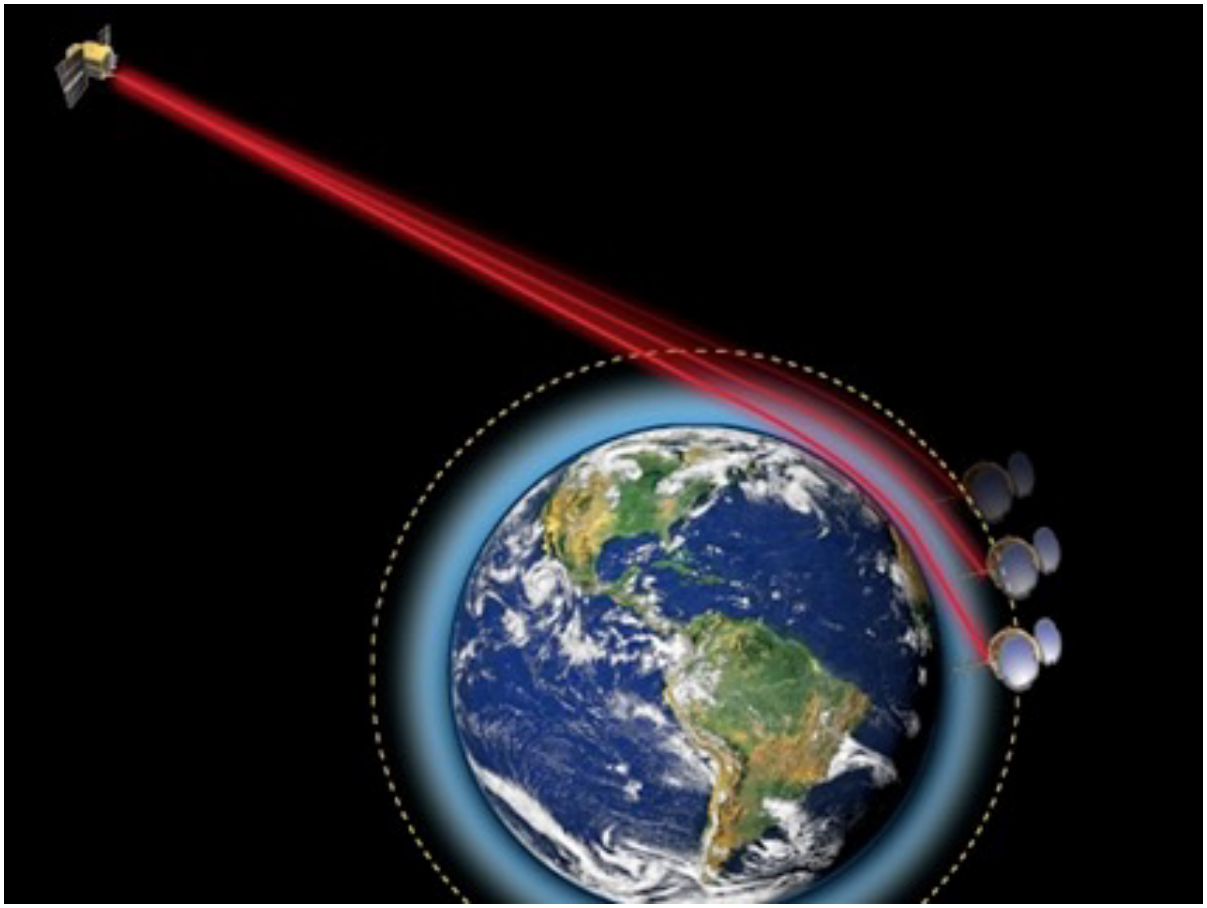

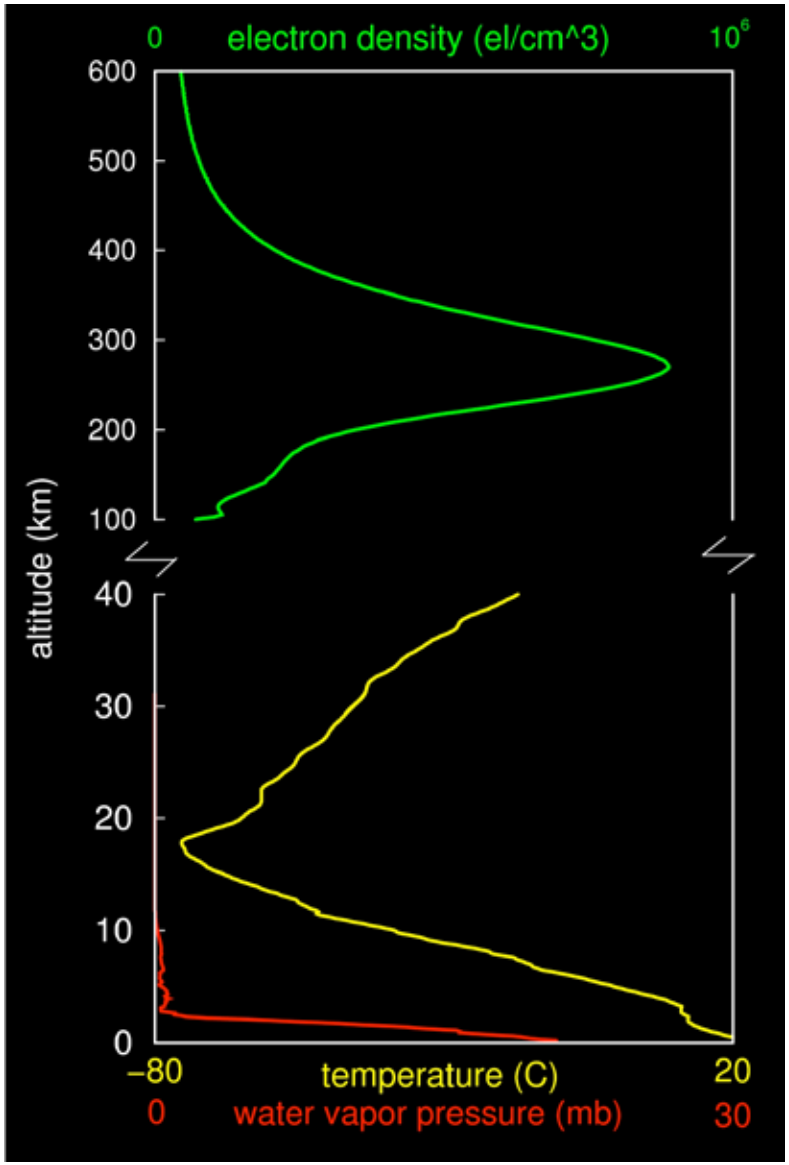

COSMIC : Constellation Observing System for Meteorology, Ionosphere, and Climate

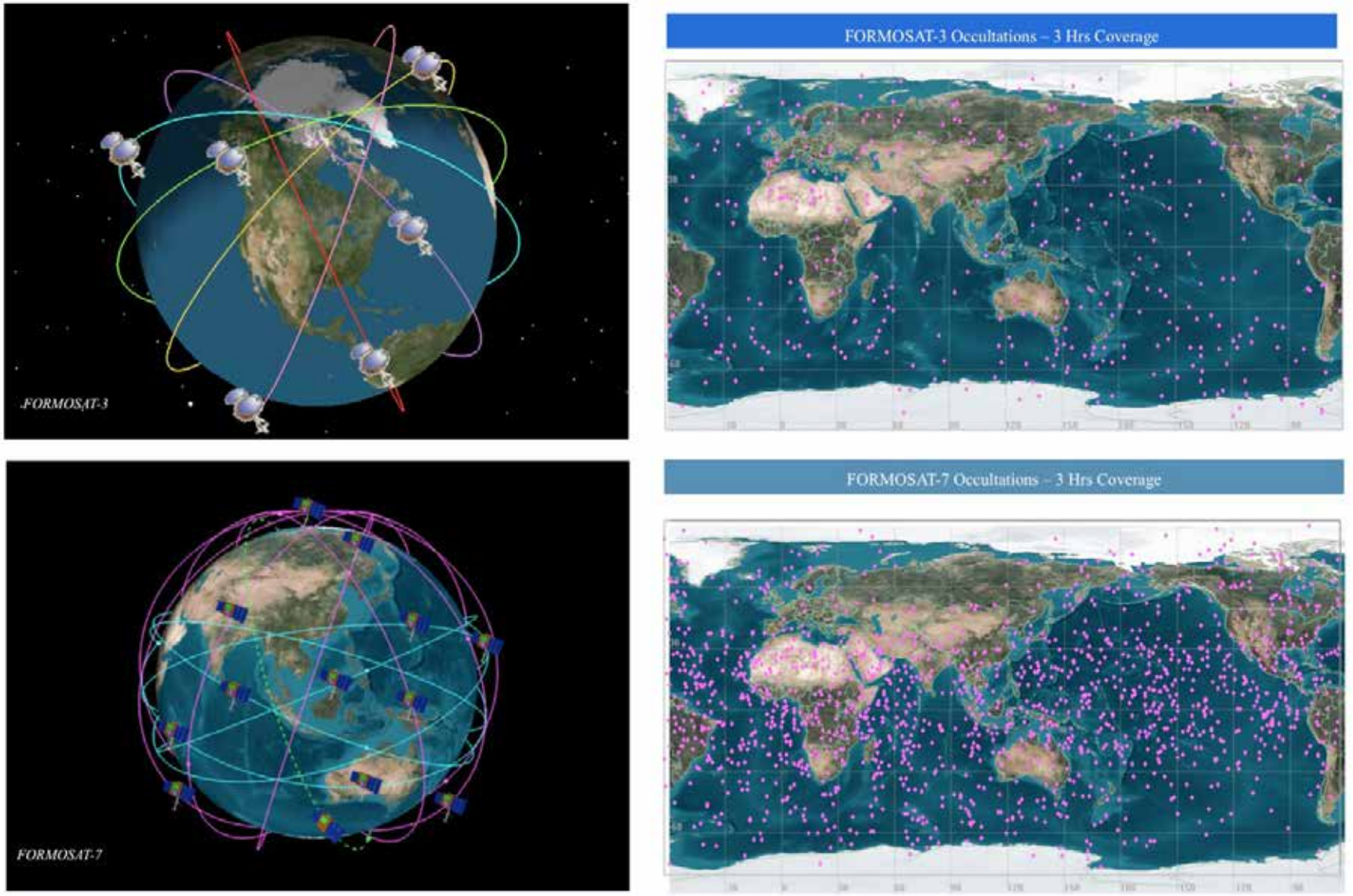

UCAR/COSMIC homepage

Fig. 1. Constellation design and estimated distribution of GPS RO soundings over a 3-h period from COSMIC/FORMOSAT-3 and COSMIC-2/FORMOSAT-7. The first tropical constellation of COSMIC-2 will be launched in 2016, and the second constellation will be launched in 2018. COSMIC-2 will provide an order of magnitude more GPS RO soundings over the tropics, which will have a significant impact on tropical cyclone prediction.

limitation of vertical resolution

$$F_n = \sqrt{\frac{n\lambda d_1 d_2}{d_1 + d_2}}, \quad d_1, d_2 \gg n\lambda,$$[3]

where

F_n is the nth Fresnel zone radius,

d_1 is the distance of P from one end,

d_2 is the distance of P from the other end,

λ is the wavelength of the transmitted signal.

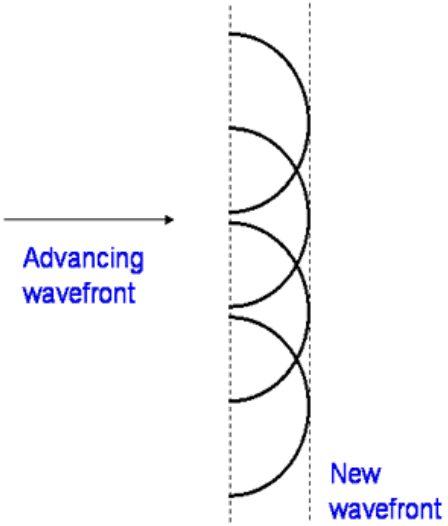

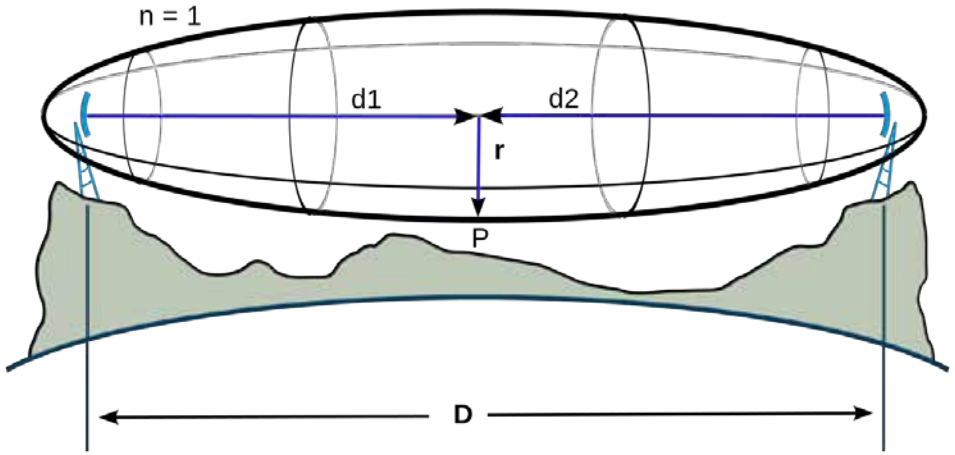

(Wikipedia)

n = 1 : First Fresnel zone. Outside this zone a destructive inference greatly reduces the contribution to the received signal.

F_1 is typically 0.5–1 km for planetary missions.

Multipath

An example of the signal spectrum time series

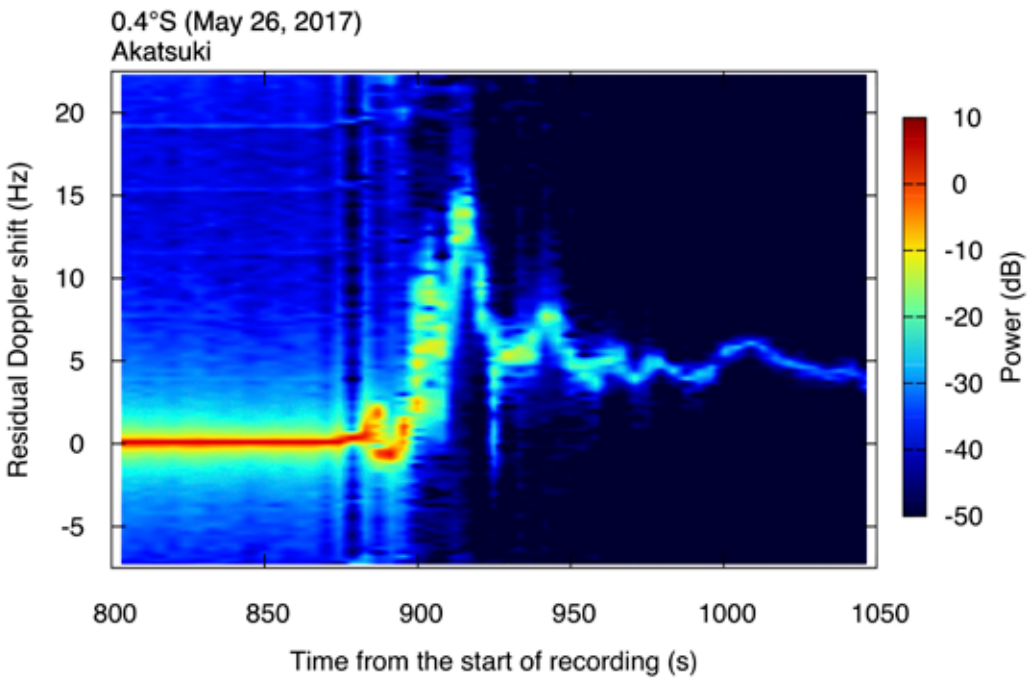

Schematic of multipath (Sokolovskiy, 2004)

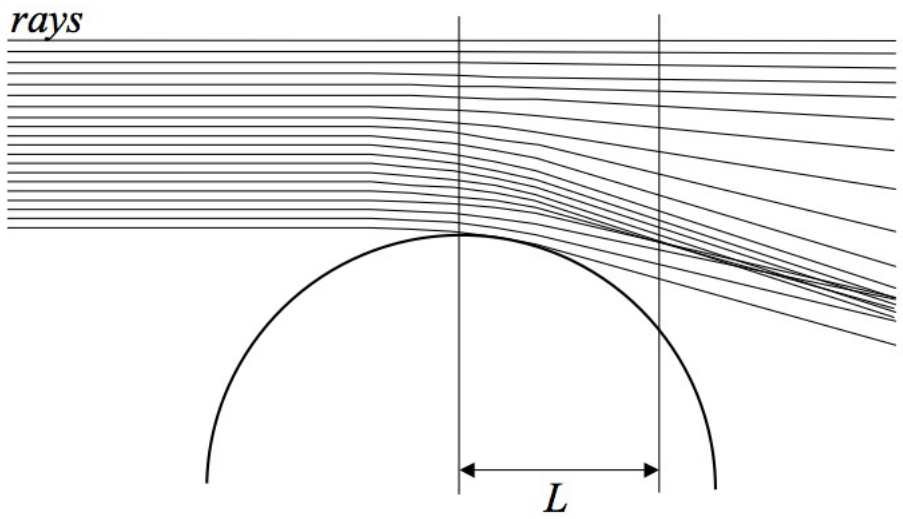

Radio holographic method can solve multipath problem (Imamura et al. 2018)

Radio holographic analysis

- One of the radio holographic methods, FSI ("Full Spectrum Inversion" Jensen et al. 2003) is applied to radio occultation data.
- Spectral analysis is applied to the entire signal at once instead of applying it to successive short time blocks.

→High vertical resolution + Disentanglement of multipath

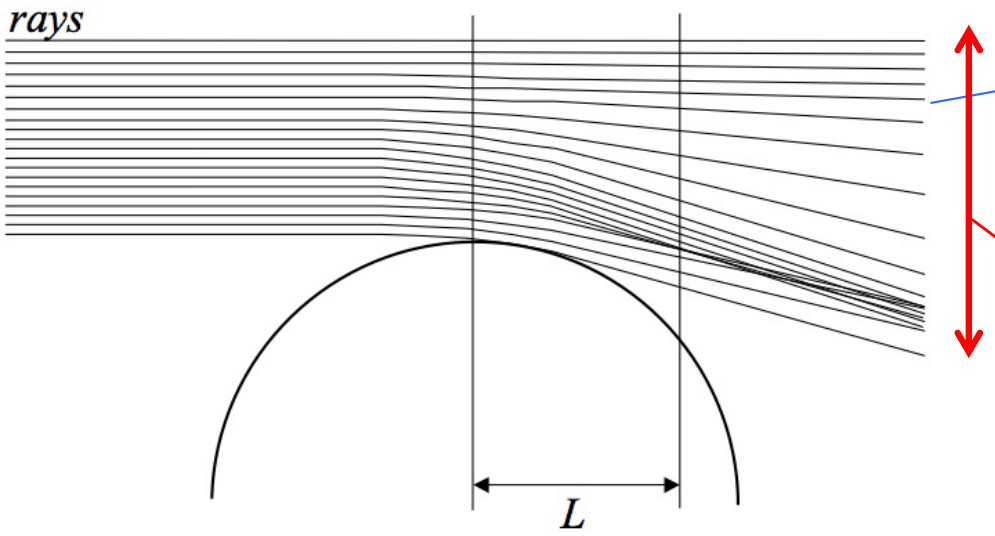

GO (geometrical optics) solves the instantaneous ray path at each time step

FSI solves the whole time series of the signal phase at once

Schematic of multipath (Sokolovskiy, 2004)

Examples

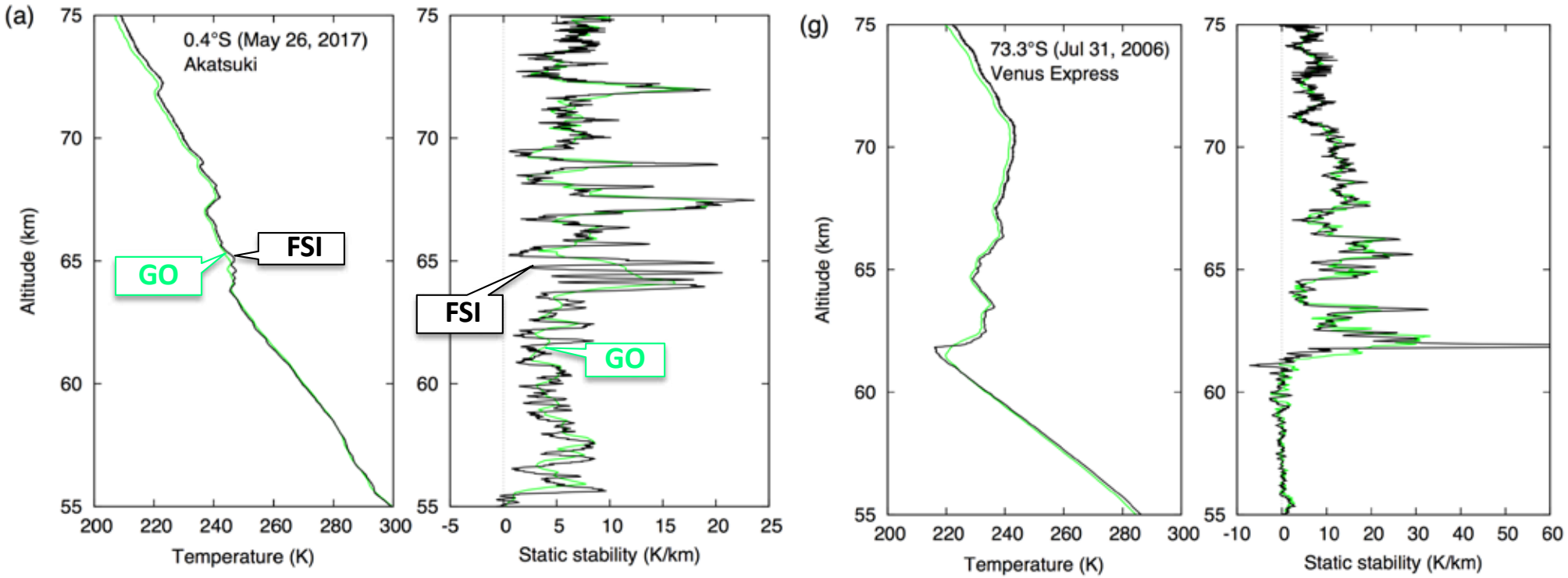

Imamura et al. (2018)

Ring occultation

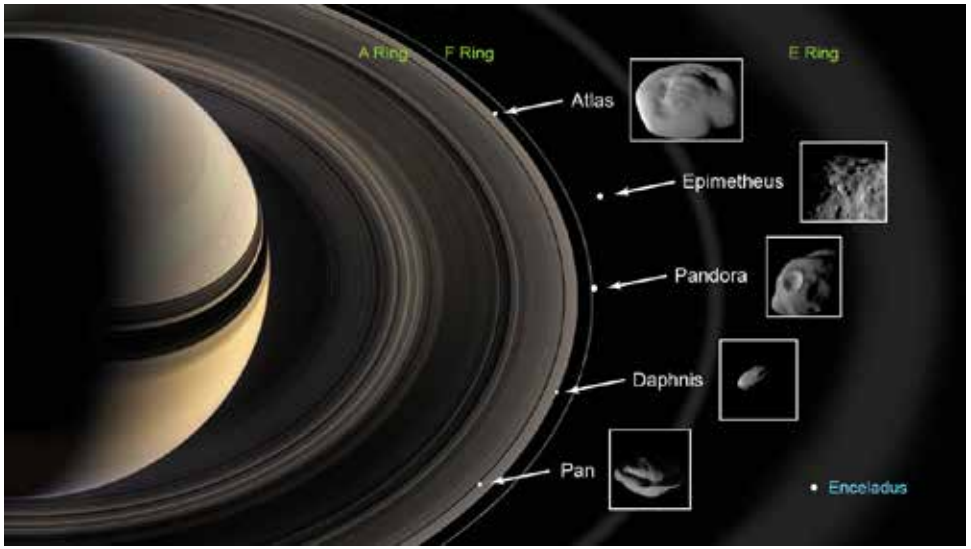

- The rings of gas giants (Jupiter, Saturn, etc) are composed of ice particles. The ring structures give clues to the history of the solar system and the dynamics of orbital revolution.
- Information to be obtained
  - Radial distribution of ring density (optical thickness) from signal intensity and phase time series
  - Particle sizes from multi-frequency measurements
- Previous observations
  - 1980 Voyager 1
  - 2004 Cassini

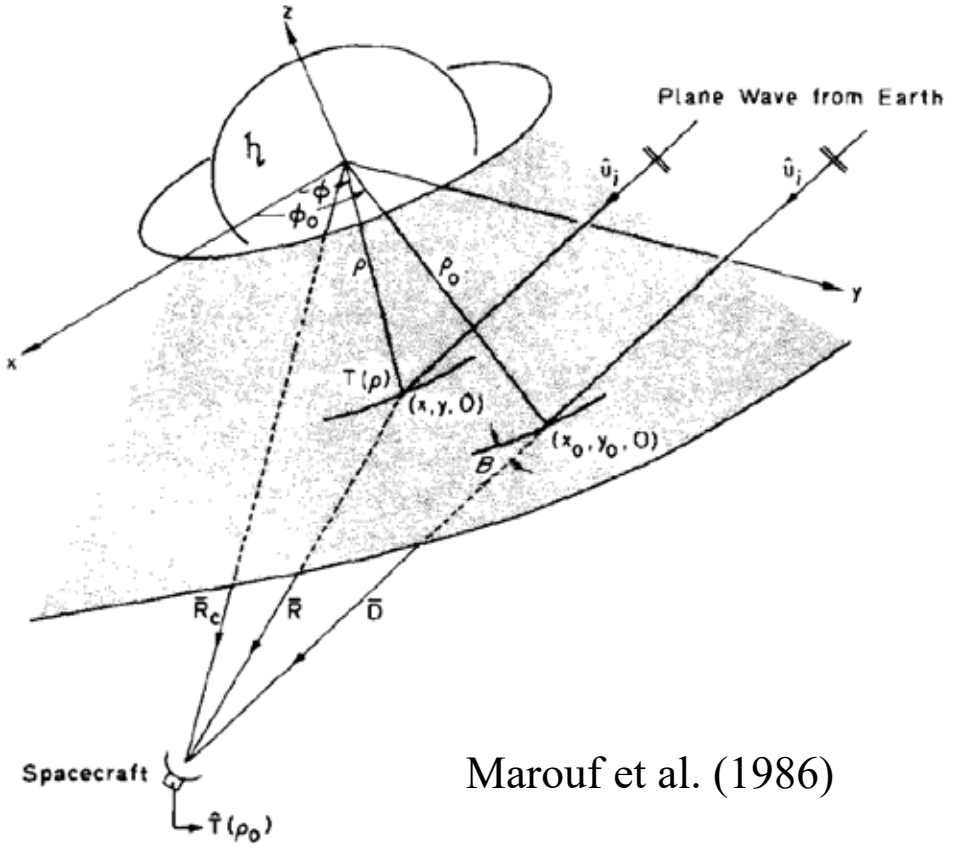

Marouf et al. (1986)

Diffraction correction by inverse Fresnel transform

Diffraction by edge of Saturn's Encke gap

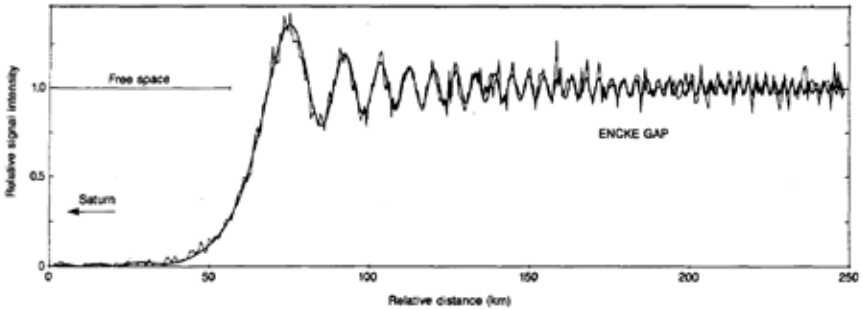

Fig. 20. Diffraction by edge of Saturn's Encke gap. Smooth, heavy curve shows theoretical diffraction from abrupt edge of grey screen with optical depth 6.5; irregular curve is observed. Horizontal scale, and hence shape of theoretical curve, is based on Voyager 1 trajectory solution; vertical scale and right-left position are obtained by least mean squares fit. Patterns match for at least 20 oscillations. (Figure from [79].)

Tyler et al. (1987)

Inversion from the measured opacity to the true opacity

$$T(\rho) = \frac{1 + i1}{2F} \int_{-\infty}^{\infty} \hat{T}(\rho_0) e^{-i(\pi/2)[(\rho-\rho_0)/F]^2} \, d\rho_0$$

True

Measured (received signal intensity)

Marouf et al. (1986)

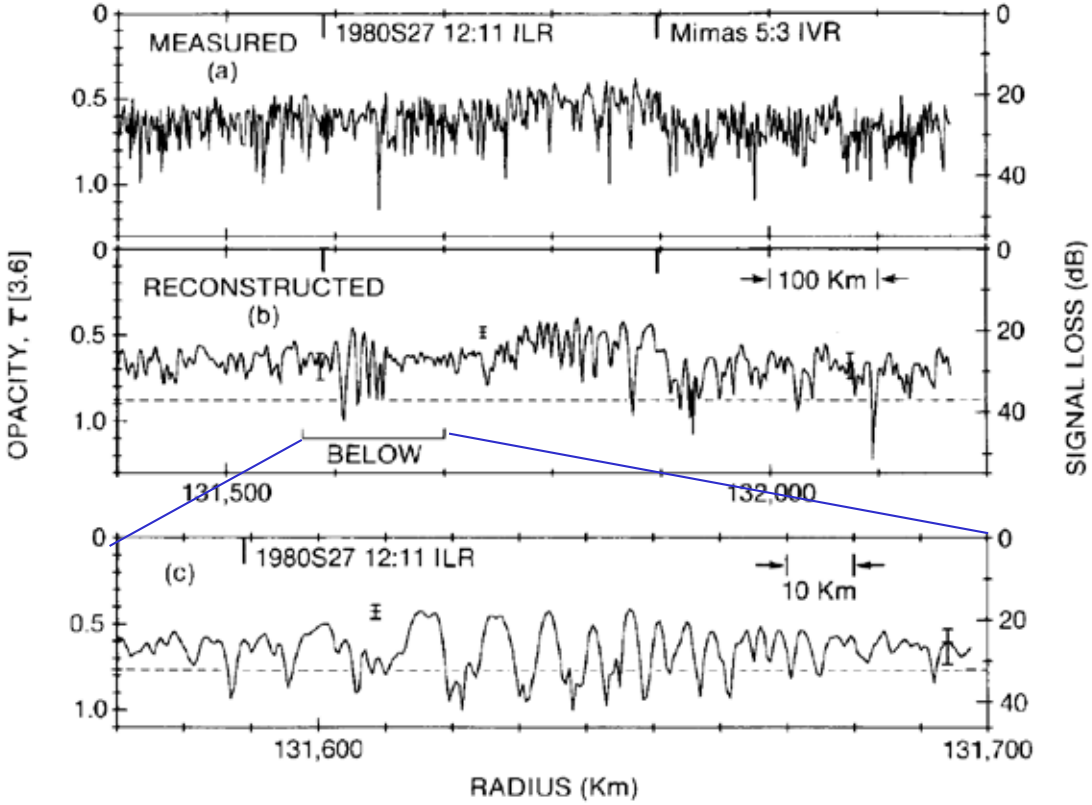

FIG. 15. (a) Measured and (b) reconstructed ($\Delta R_\phi \approx 2.5$ km, $\lambda = 3.6$ cm) opacity profiles of a region 800 km wide in Ring A encompassing the 1980S27 12:11 density wave and the Mimas 5:3 bending wave. Theoretical locations of corresponding resonances are as indicated. Both waves are effectively masked in the initial diffraction-limited measurement. Note that the envelope of opacity minima of the bending wave is at a level noticeably smaller than the mean opacity level outside the wave region. (c) Many more oscillations of the density wave are revealed at 900 m effective resolution. Note that regions of opacity maxima are almost completely masked by noise at this resolution, however.

High-resolution radial profiles

Numerical simulation of a density wave

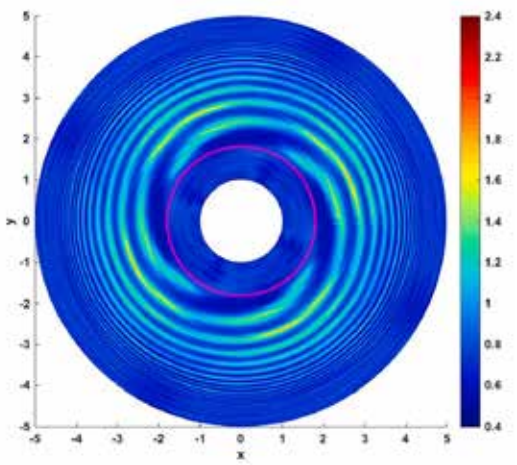

Rappaport et al. (2021)

Sub-km (~200 m) radial resolution

Cassini

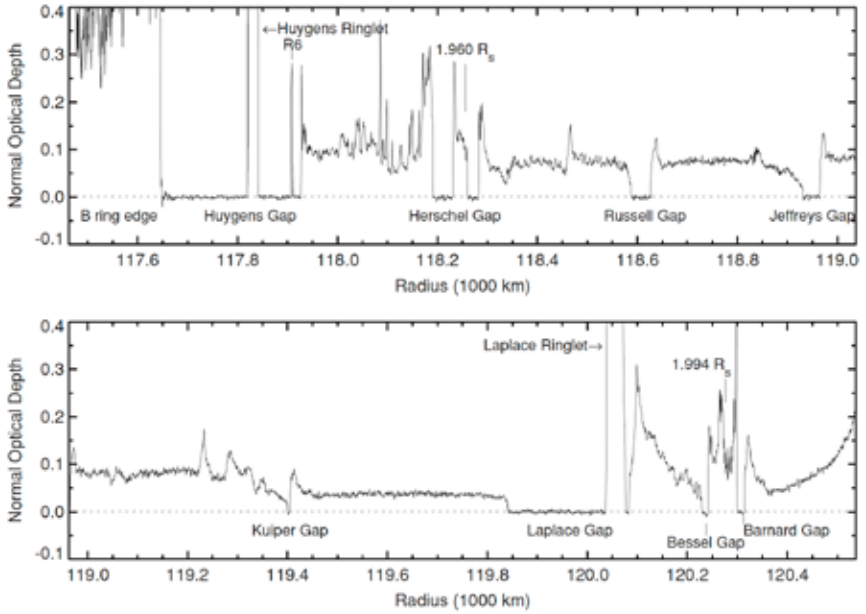

French et al. (2010)

Density wave

Marouf et al, (1986)

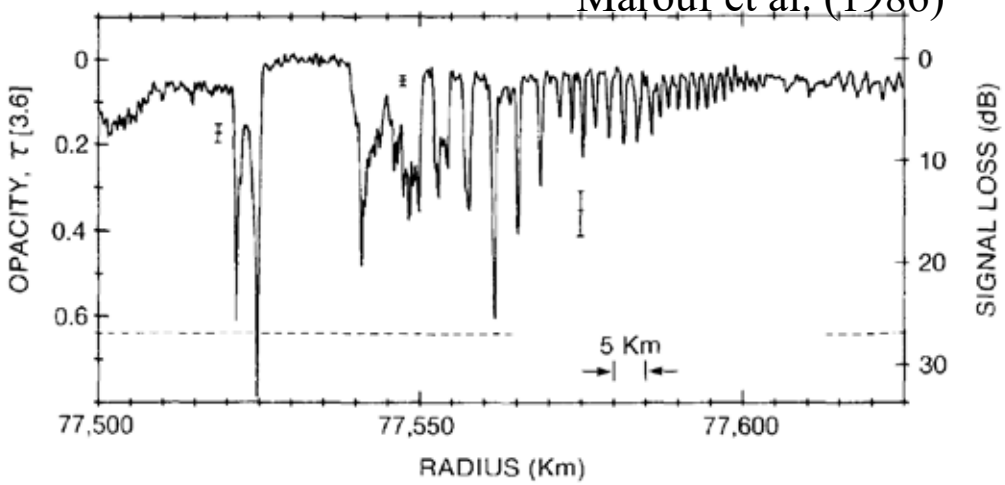

Density waves are spiral patterns generated by resonances with either Saturn's moons or structures inside the planet

Radio occultation of the solar wind

- High-speed tenuous plasma flowing from the Sun
- Impact on "space weather" and planetary evolution

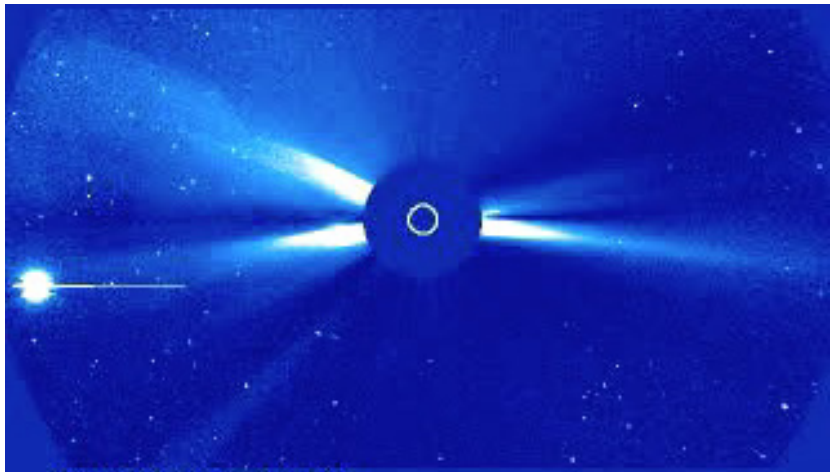

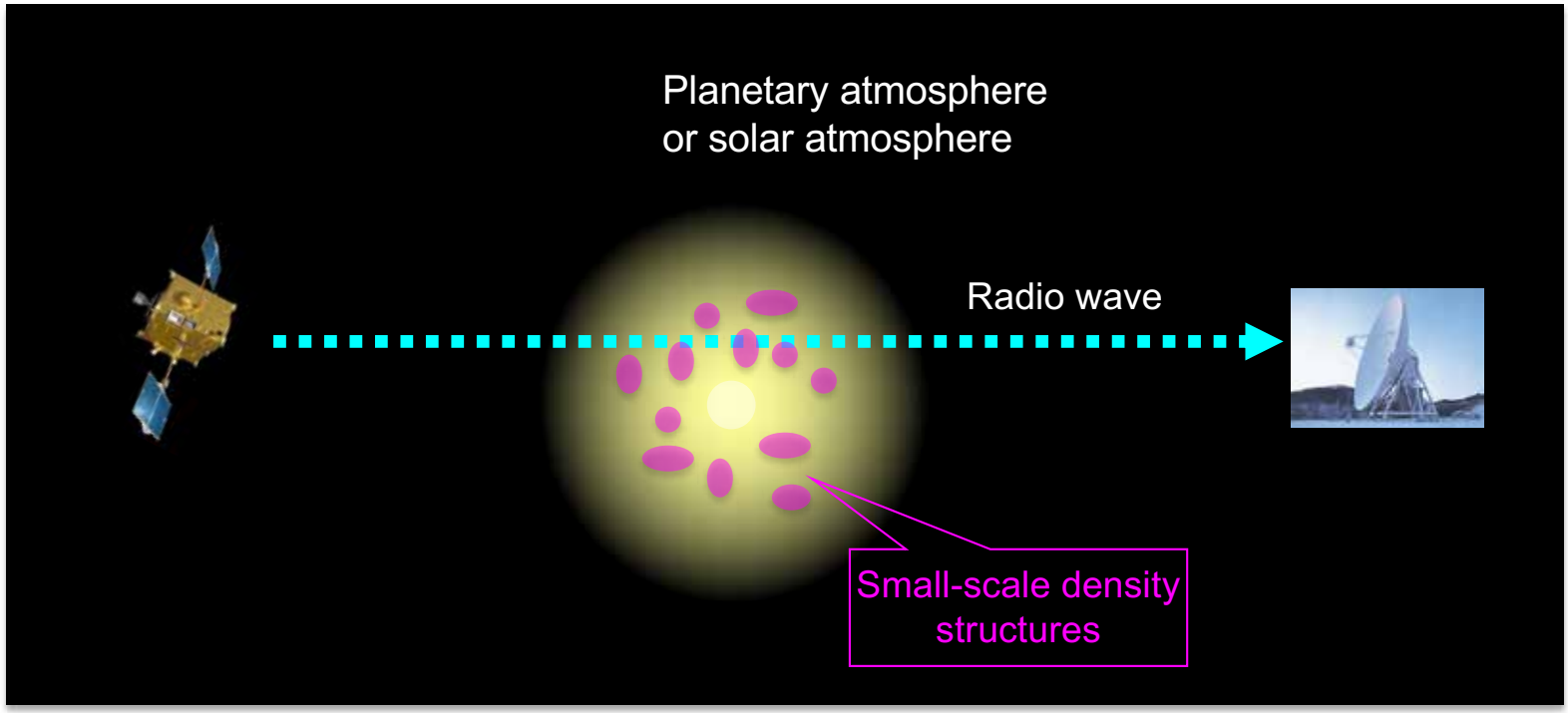

Intensity scintillation

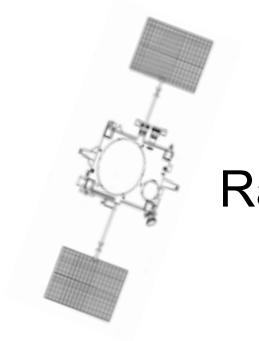

Radio wave

Plane wave

Movement of phase modulator relative to the ray path

Solar wind

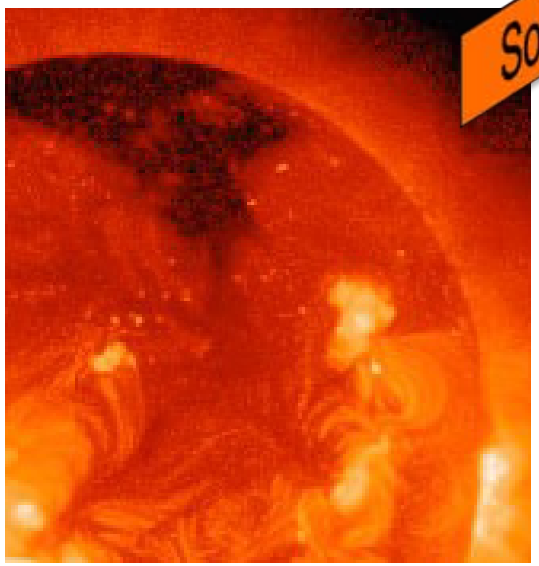

Phase modulating ‘screen’

Disturbed wave front

Diffraction pattern projected onto a screen (observer)

Fast wind and Slow wind

Observations in 2011
(Imamura et al. 2014, ApJ)

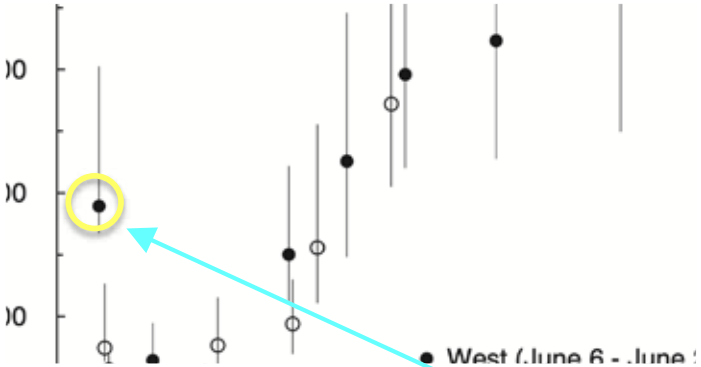

Observations in 2016
(Chiba et al., 2022)

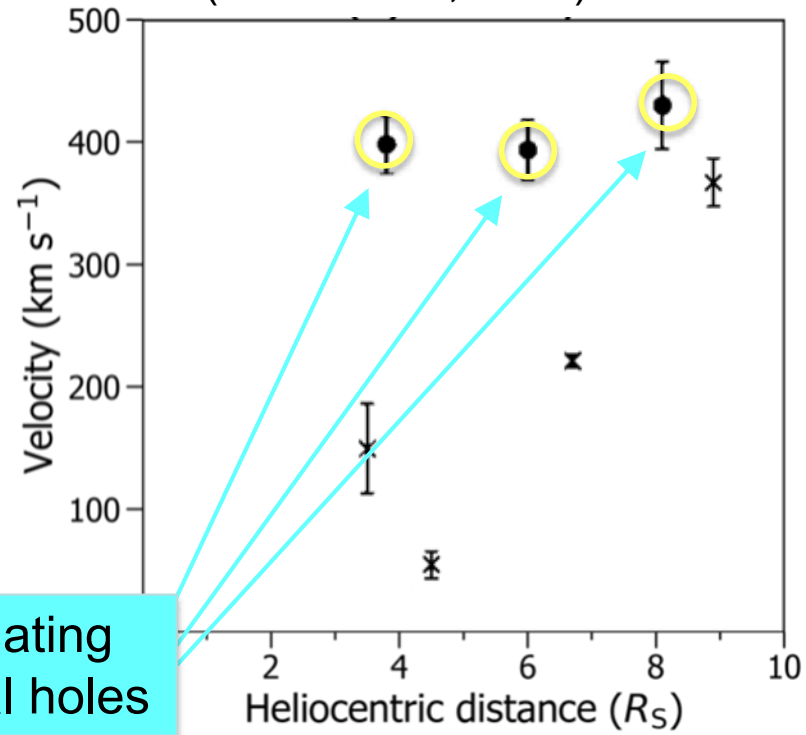

Flows originating
from coronal holes

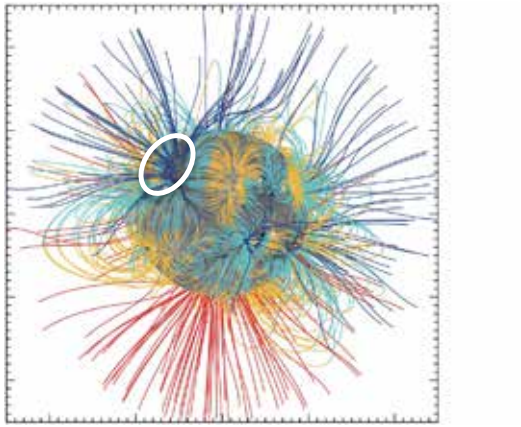

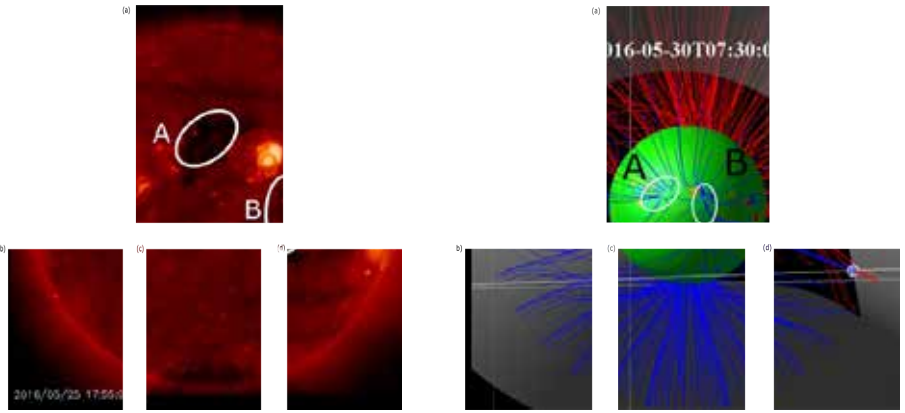

Phase/frequency fluctuation

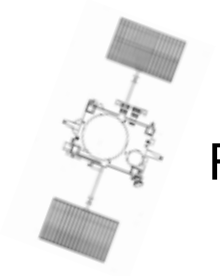

Radio wave

Movement relative to the ray path

Plane wave

Solar wind

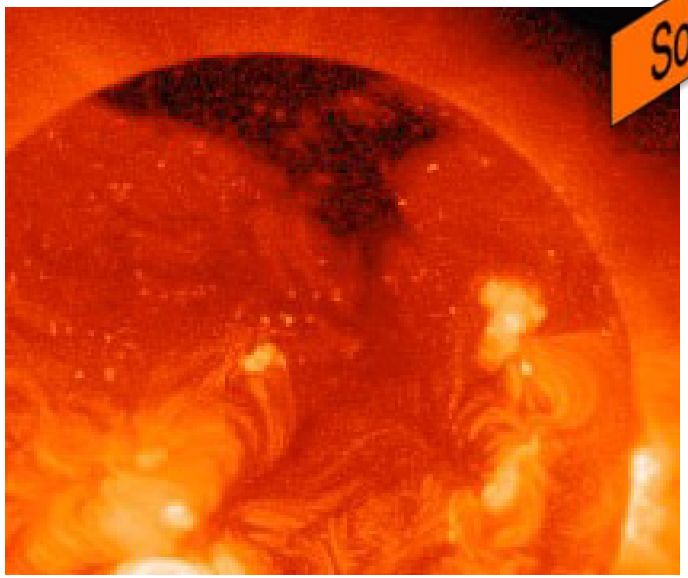

Density modulation

Phase modulation

ground antenna

Radial distribution of acoustic waves

Wavelet analysis
(Miyamoto et al. 2014, ApJ)

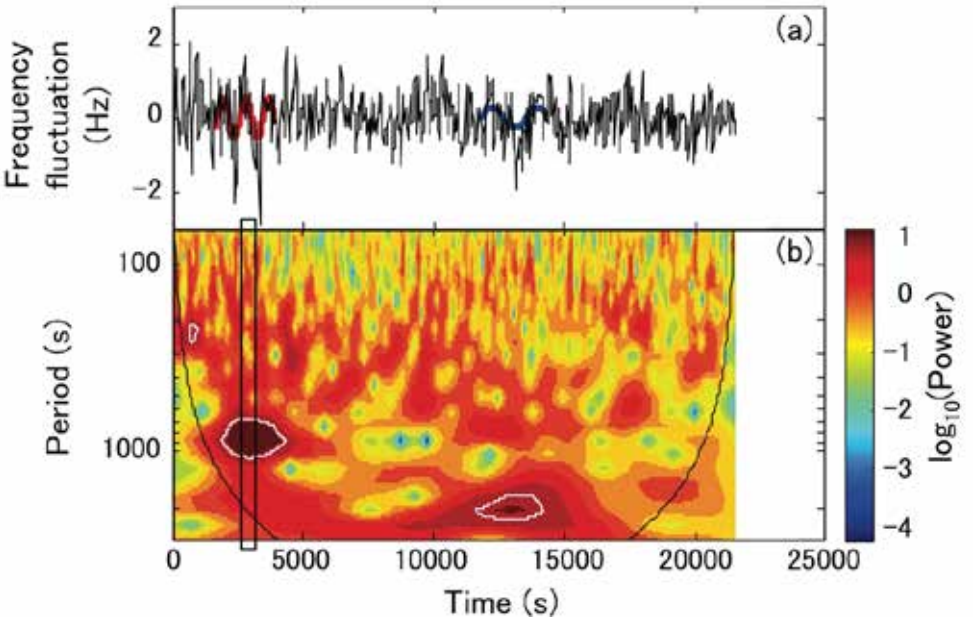

Local generation of large-amplitude acoustic waves ?

$\frac{n'}{n_0}$

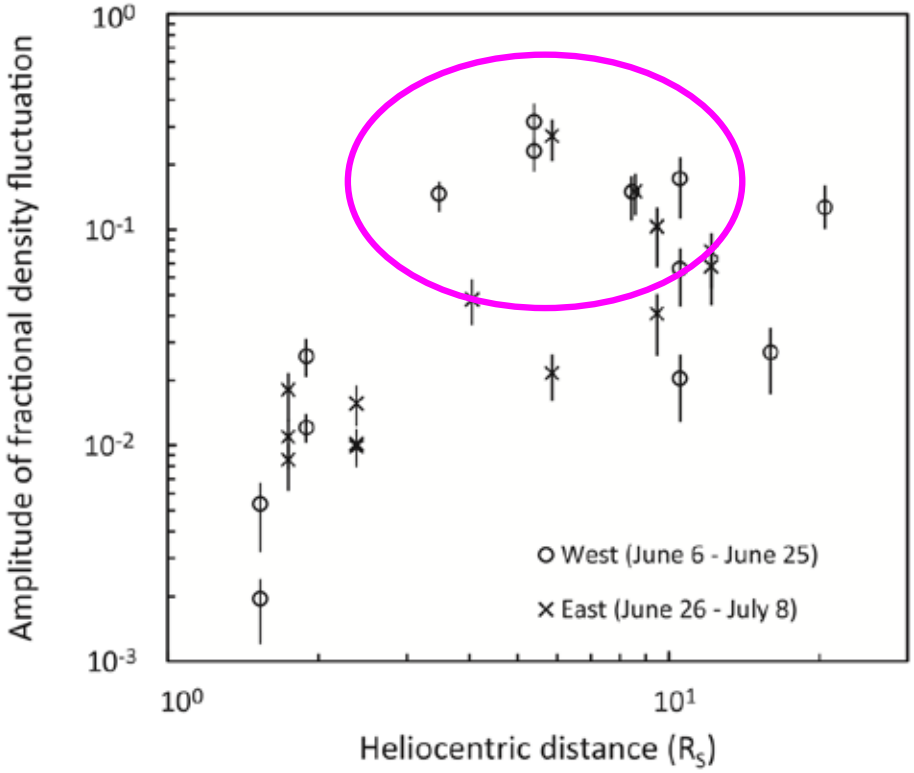

- The radial distribution suggests local generation of acoustic waves in the extended corona, probably through nonlinear dissipation of Alfvén waves that propagated from the photosphere.
- The dissipation of these waves will play key roles in coronal heating.

Doppler tracking of spacecraft to measure gravity anomaly

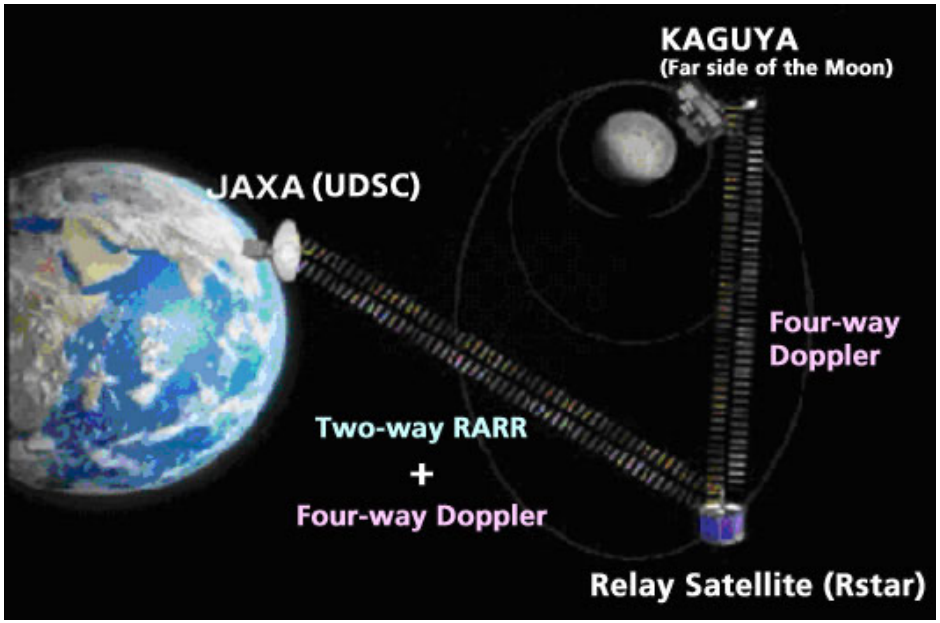

4way Doppler measurement using Relay satellite

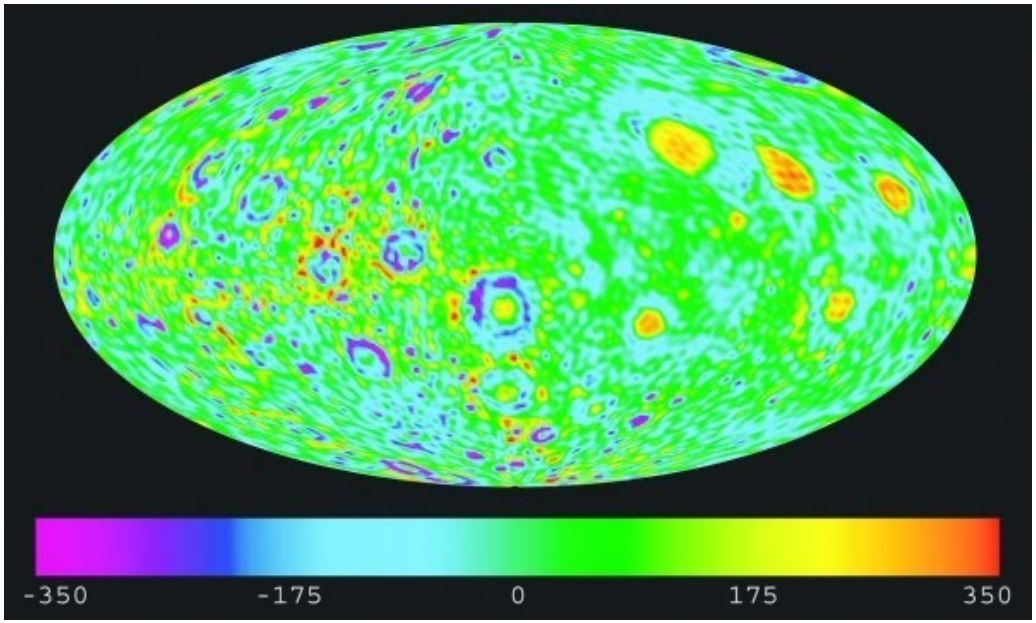

Gravity anomaly map of the Moon's surface obtained by JAXA's SELENE mission (in mGal = 10^{-5} m/s^2)

Doppler tracking of Juno spacecraft

- The spacecraft acts as a test particle falling in the gravity field of the planet. Jupiter's gravity is inferred from range-rate measurements between a ground antenna and the spacecraft during perijove passes.
- The ground station transmits two carrier signals, at 7,153 MHz (X band) and 34,315 MHz (Ka band). On board, an X-band transponder and a Ka-band frequency translator lock the incoming carrier signals and retransmit them back to the ground station at 8,404 MHz and 32,088 MHz, respectively. The range-rate (Doppler) observable is obtained by comparing the transmitted and received frequencies.
- Spherical harmonics representation of planetary gravity fields is determined by the density distribution inside the body.

Doppler tracking of Juno spacecraft

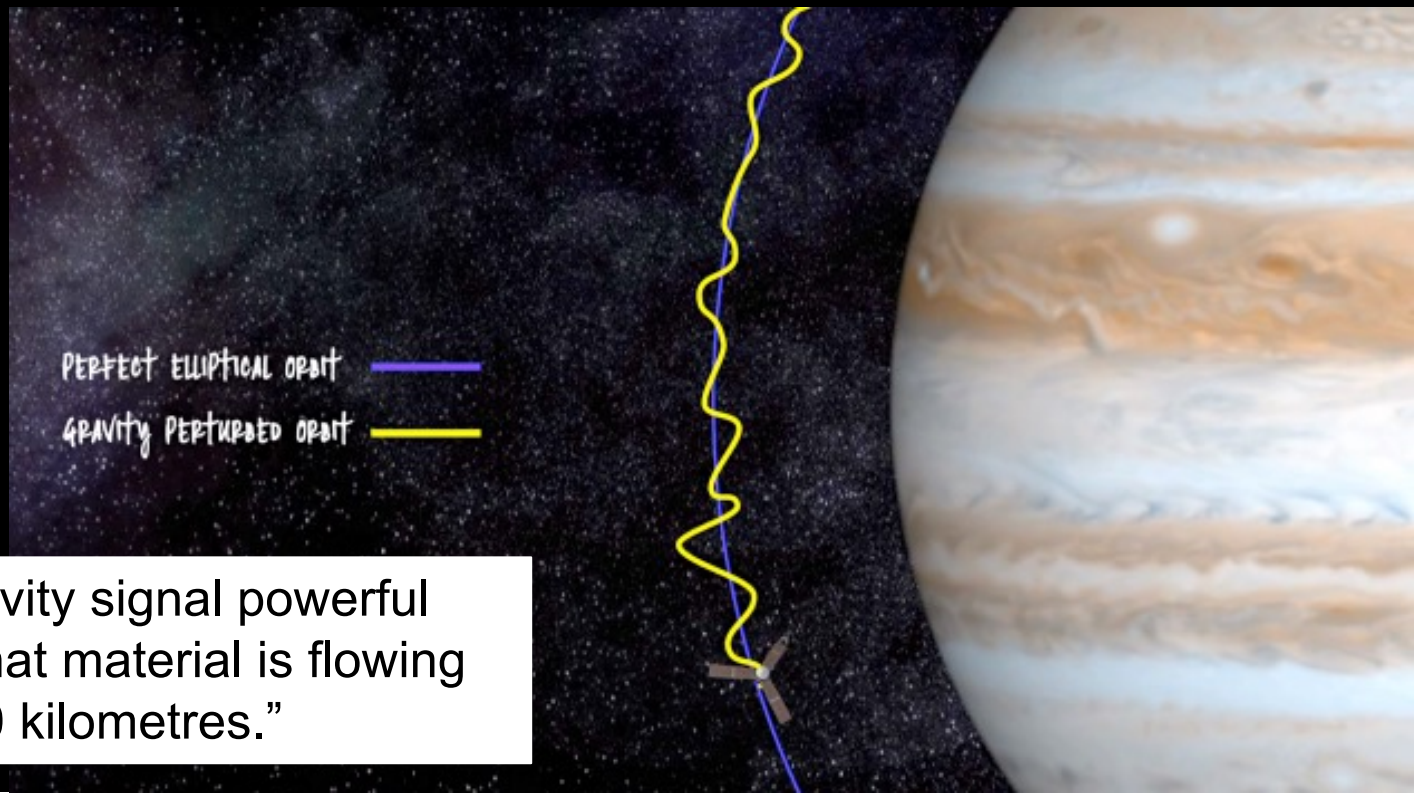

"Juno detected a gravity signal powerful enough to indicate that material is flowing as far down as 3,000 kilometres."

Less et al. (2018)

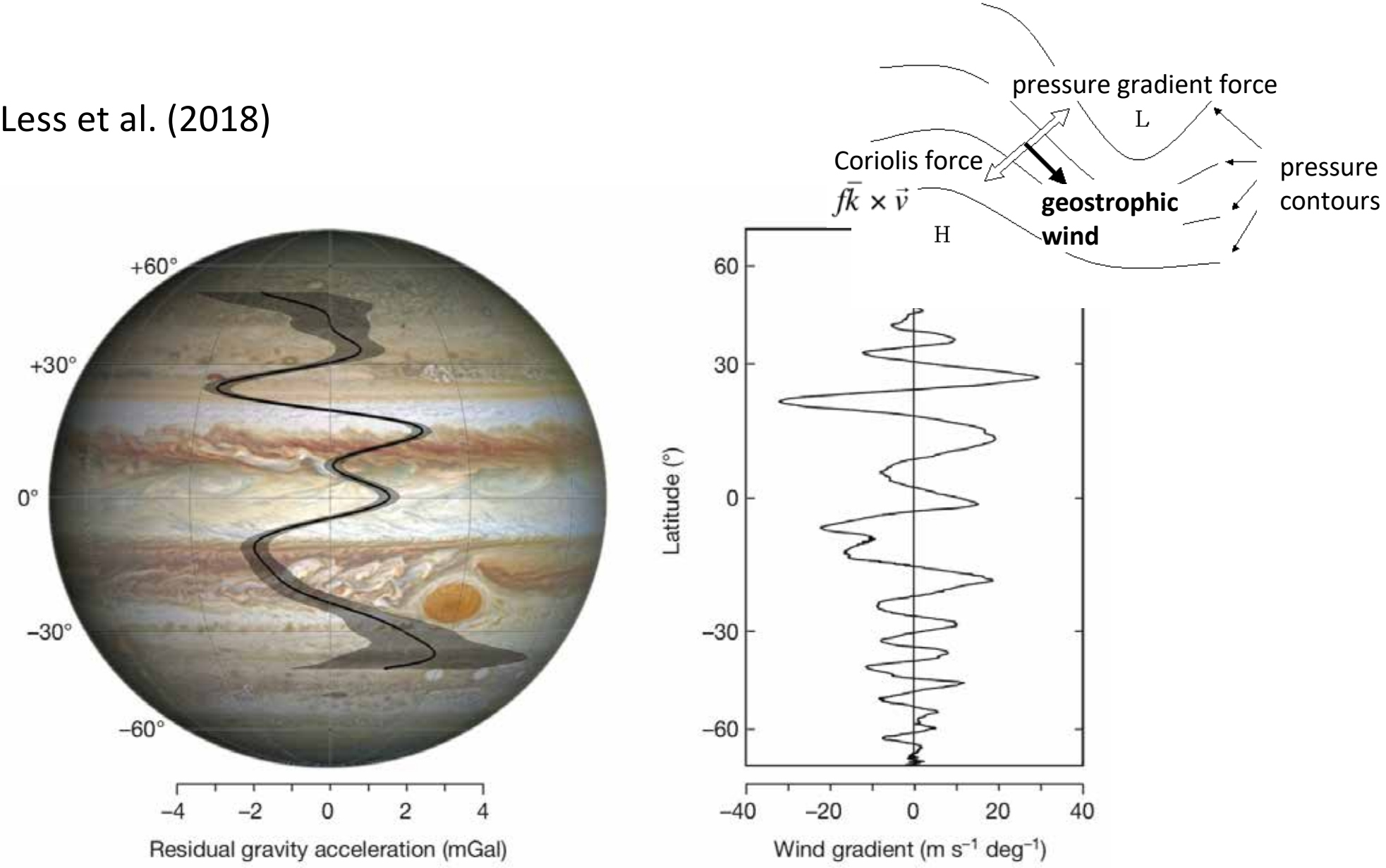

“The observed jet streams, as they appear at the cloud level, extend down to depths of thousands of kilometres beneath the cloud level, probably to the region of magnetic dissipation at a depth of about 3,000 kilometres”

Taylor–Proudman theorem

- In a fluid that is steadily rotated, the fluid velocity will be uniform along any line parallel to the axis of rotation.

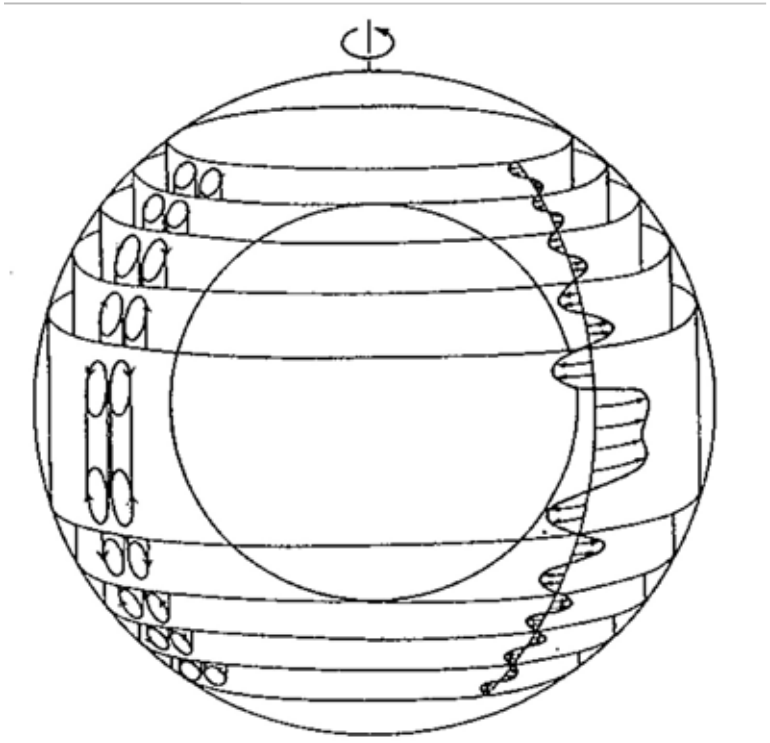

Busse (1994)

Momentum equation in rotational frame

$$\frac{d\vec{v}}{dt} + 2\vec{\Omega} \times \vec{v} + \frac{1}{\rho}\nabla p + \nabla\Phi = 0$$

Assuming non-compressivity and d/dt=0, the curl is applied to give

$$\vec{\Omega} \cdot \nabla\vec{v} = 0$$

Taking z-axis along the planet's rotational axis,

$$\frac{\partial\vec{v}}{\partial z} = 0$$

Microwave radiometer

JUNO/MWR

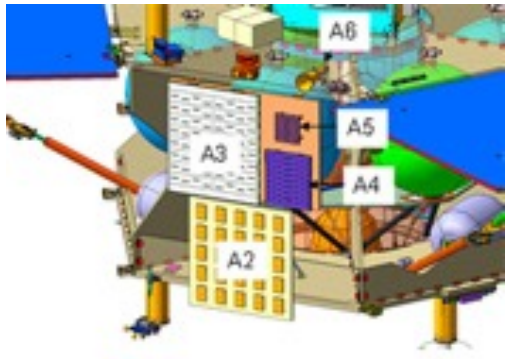

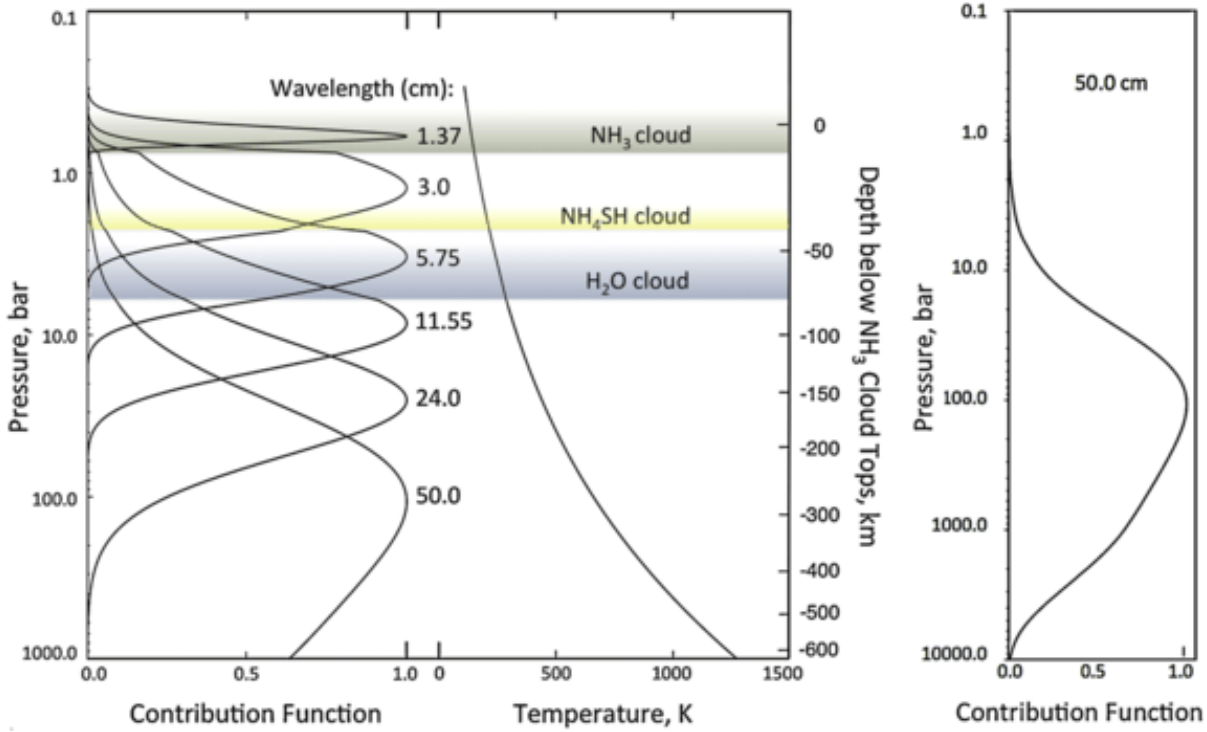

- Six antennas measure radio waves at frequencies 600 MHz, 1.2, 2.4, 4.8, 9.6 and 22 GHz
- Abundance of water and ammonia (NH_3) in the deep layers of the atmosphere up to 500–600 km deep
- The combination of different wavelengths and the emission angle should make it possible to obtain a temperature profile at various levels of the atmosphere.

Li et al. (2017)

NH_4 concentration (in ppm)

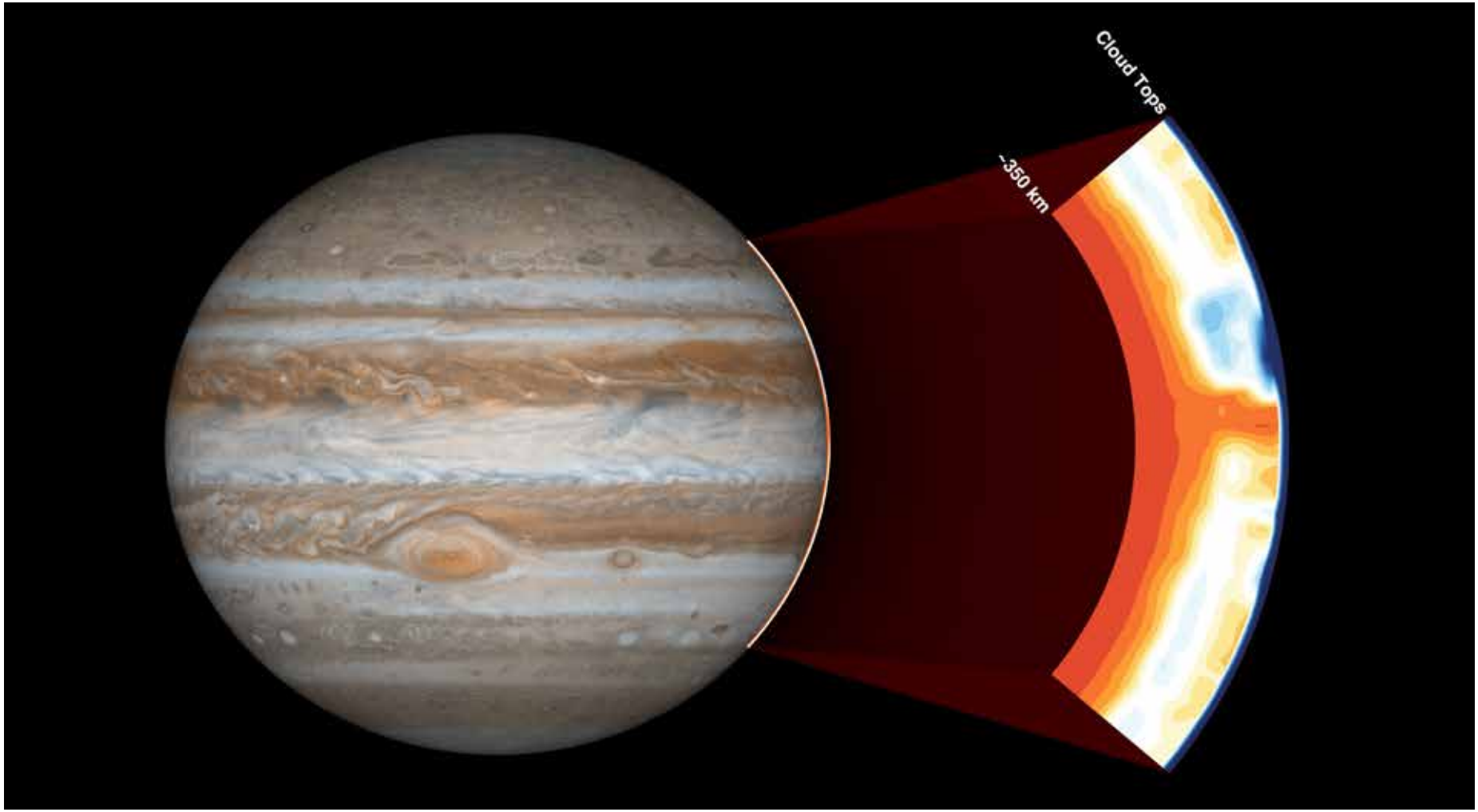

Figure 4. The colored contours show the ammonia concentration in parts per million inverted from nadir brightness temperatures during PJ1 flyby assuming that the deep water abundance is 0.06% (0.65 times solar). The deep ammonia abundance is 373 ppm, and the reference temperature is 132.1 K at 0.5 bar. The aspect ratio in the horizontal and vertical is exaggerated.

Planetary images

- The contrast in an original image is dominated by geometrical (illumination) effects. To visualize the detail of the surface, the effects need to be removed.

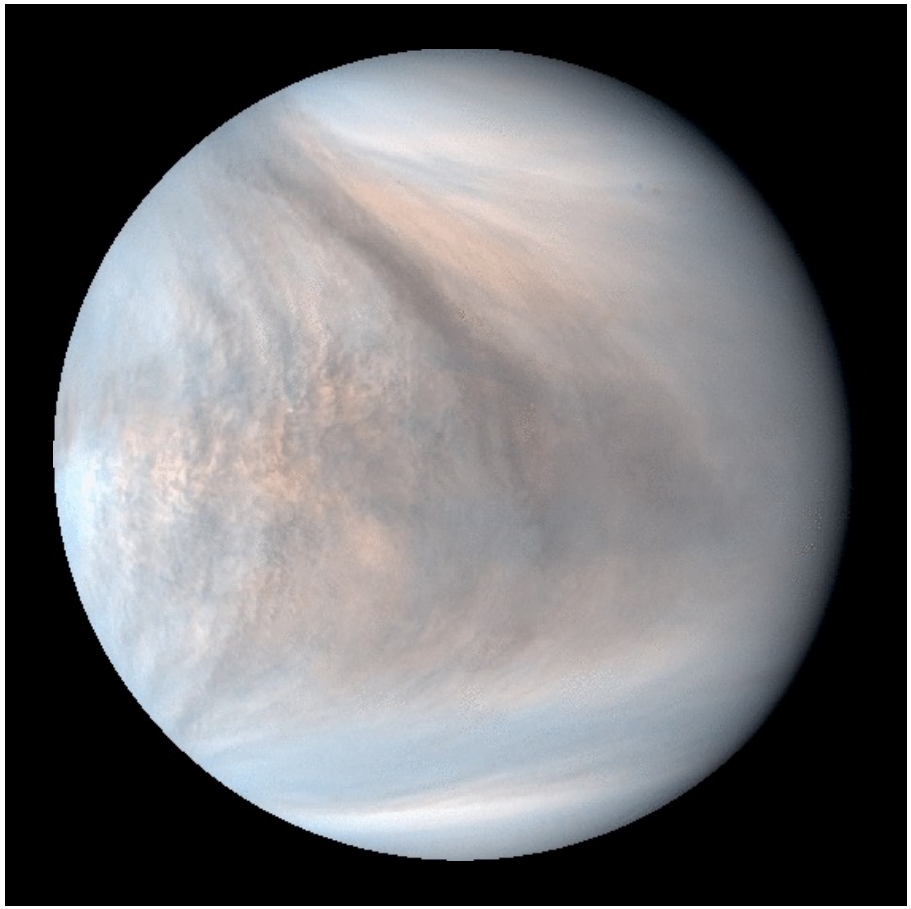

UV image of Venus taken by Akatsuki

Photometric correction

- The incident solar flux at each position on the planetary surface is proportional to the cosine of the incidence angle.
- The illumination effect can be roughly removed by dividing the original image by the model image, which is cosine of the incidence angle. (In real applications, more complicated model is used.)

Original image

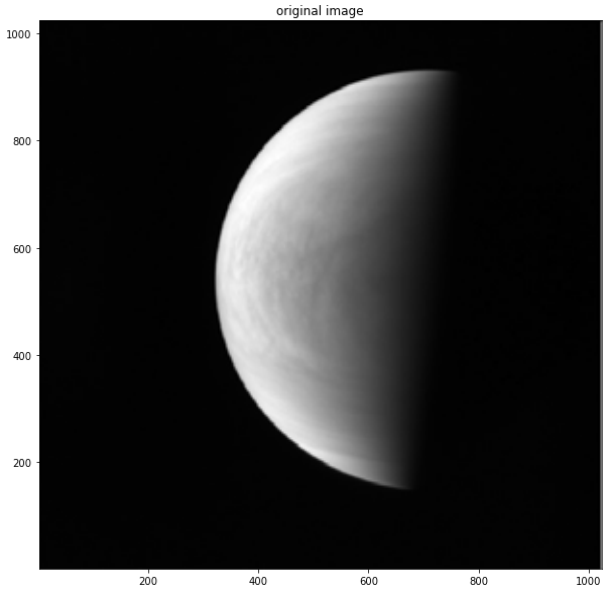

÷

cos θ

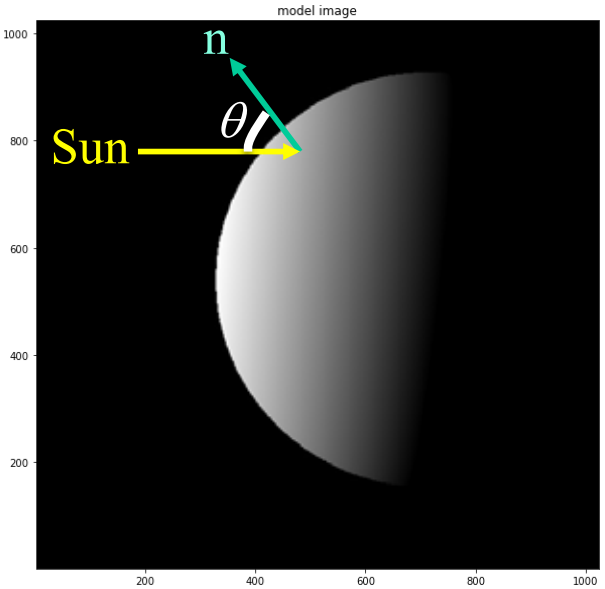

=

Corrected image

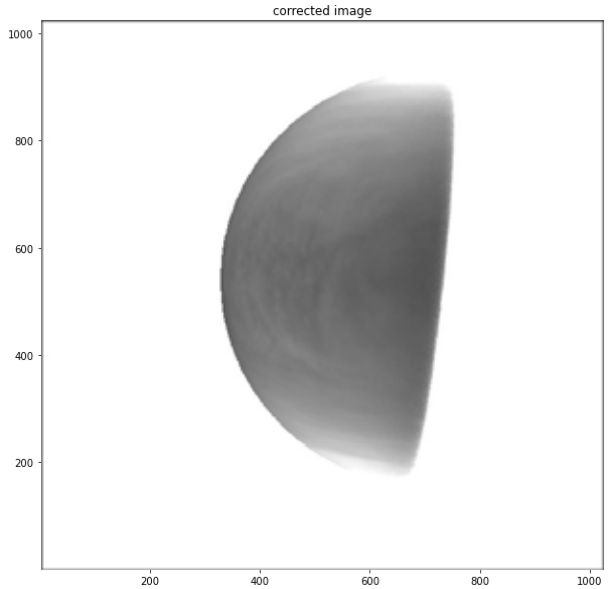

High-pass filtering

- To see the details of the surface, high-pass filtering is frequently used.
- High-pass filtering can be done by subtracting a smoothed image from the original (corrected) image. Moving average (running average) with a Gaussian function is frequently used for smoothing.

Corrected image

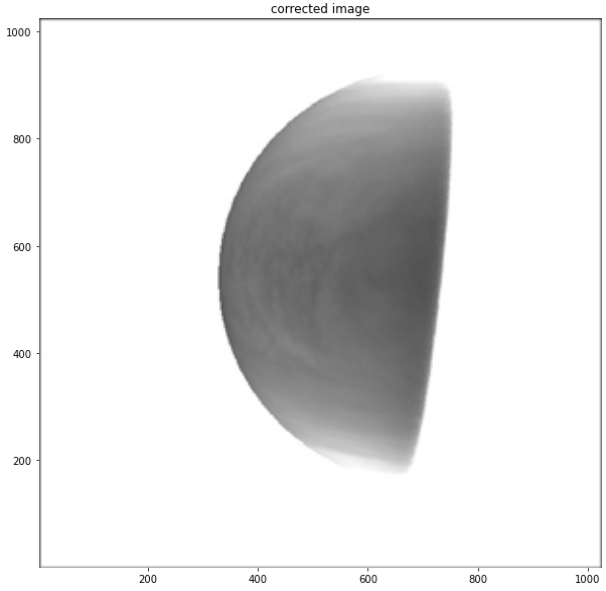

Smoothed image

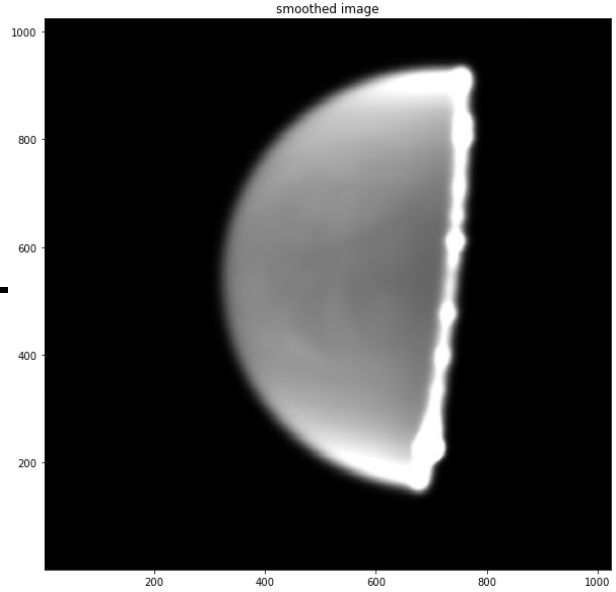

Filtered image

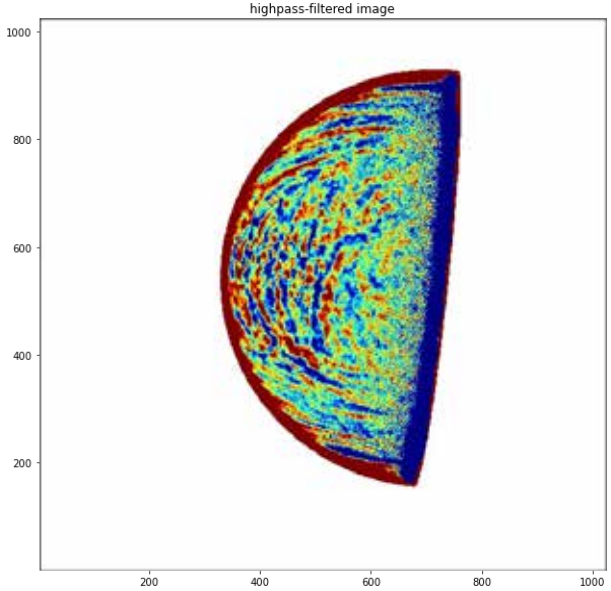

Ellipse fitting to precisely determine the camera pointing accuracy

- The accuracy of the pointing direction of onboard cameras measured by the spacecraft is insufficient in many cases.
- The pointing information can be corrected by fitting an ellipse to the limb of the planet.

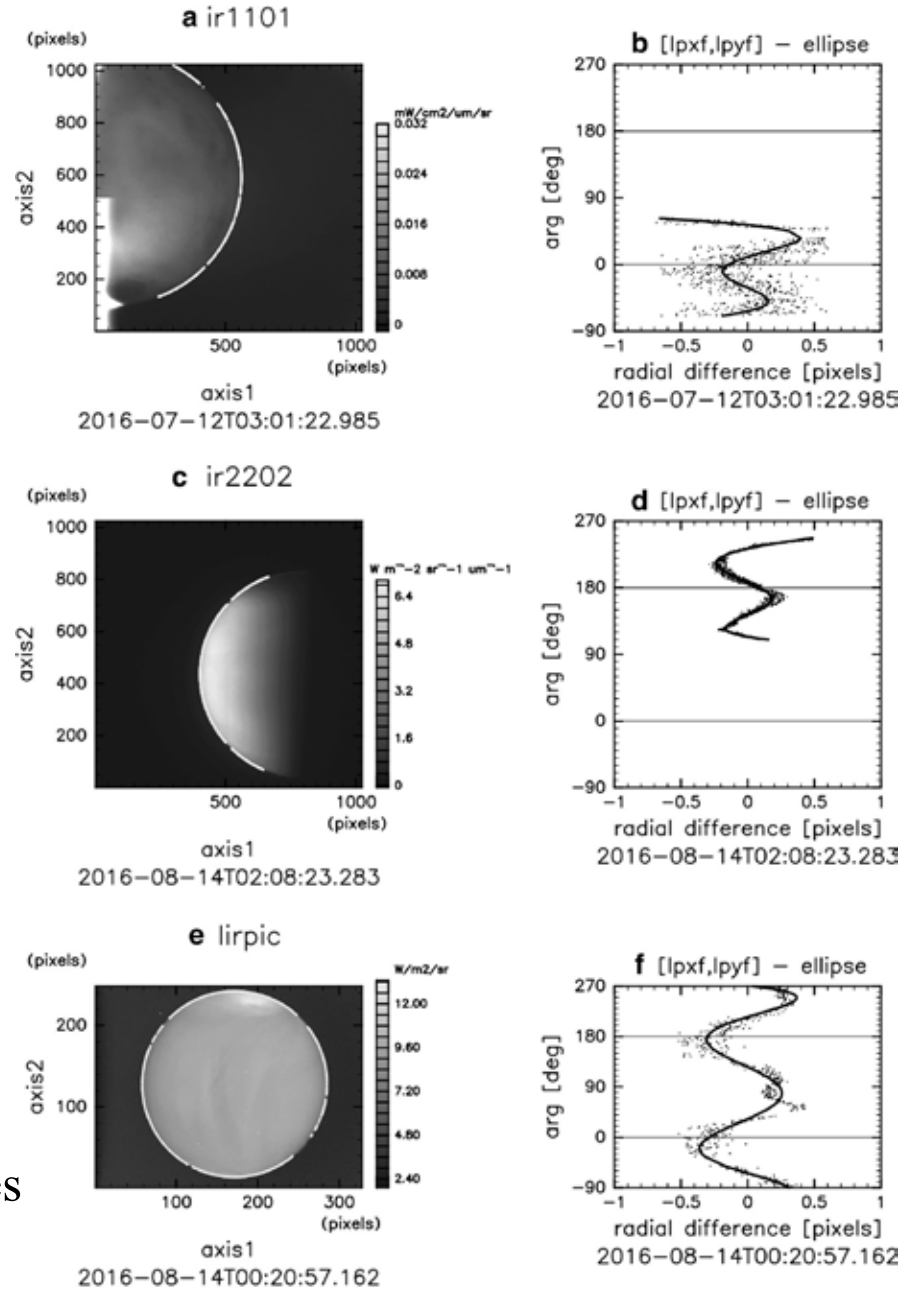

Ellipse fitting to Venus images (Ogohara et al. 2017)

Projection onto planetary coordinate

- Movement of the atmosphere can be observed by projecting successive images onto the planetary coordinate.

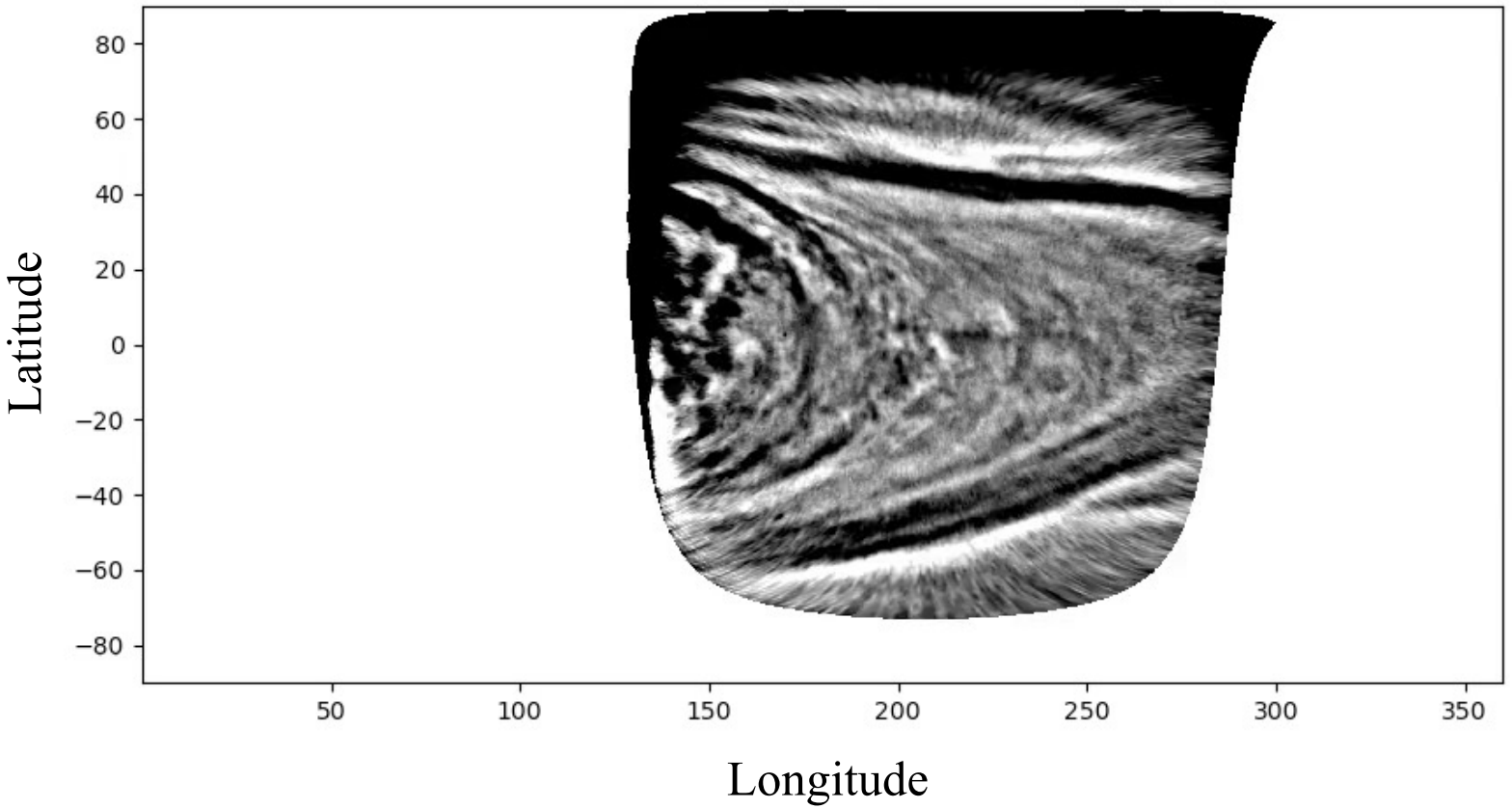

Cloud tracking with cross-correlation method

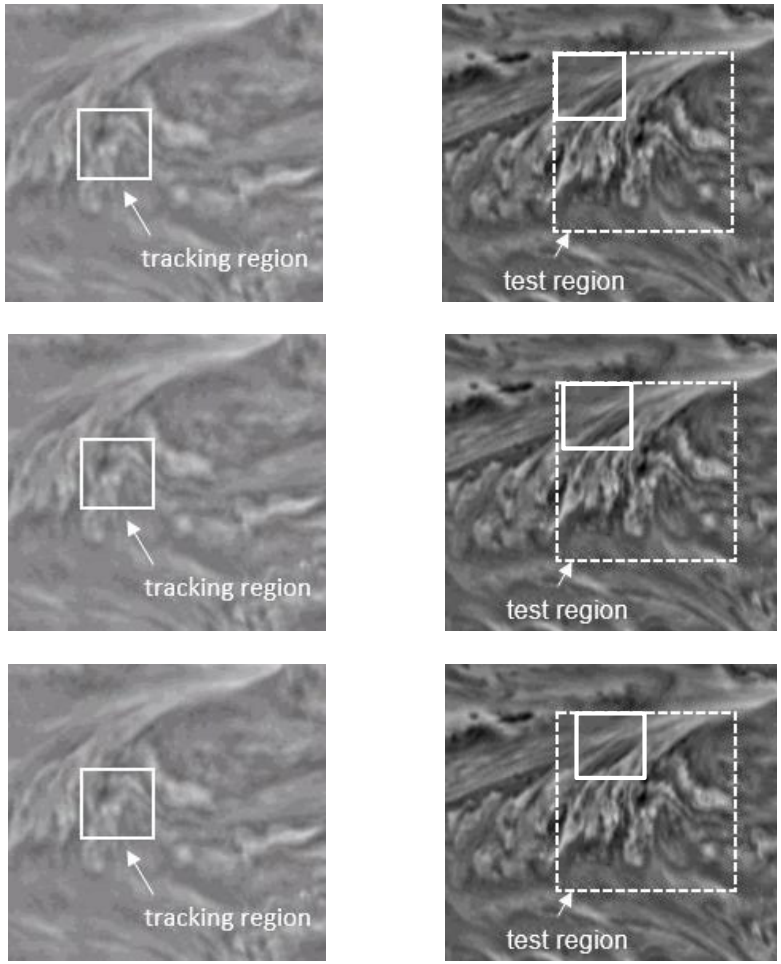

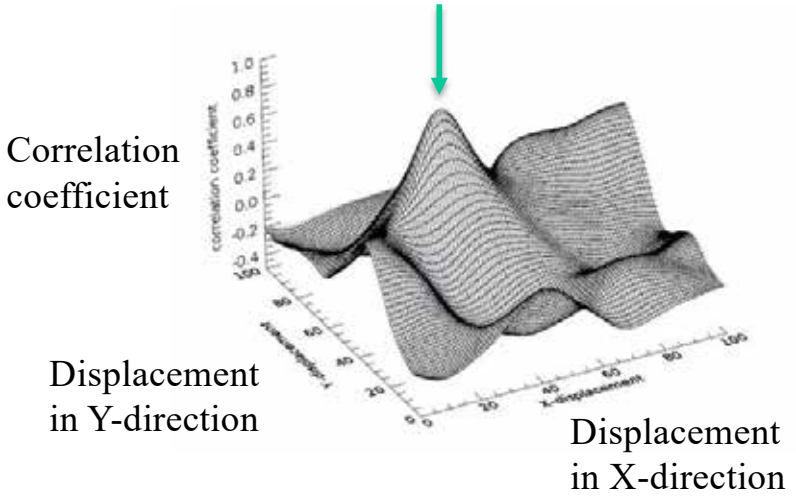

- The peak position on the correlation surface gives the displacement vector.
- Division the displacement by the time interval gives the velocity vector.

Cloud-tracked winds

Earth

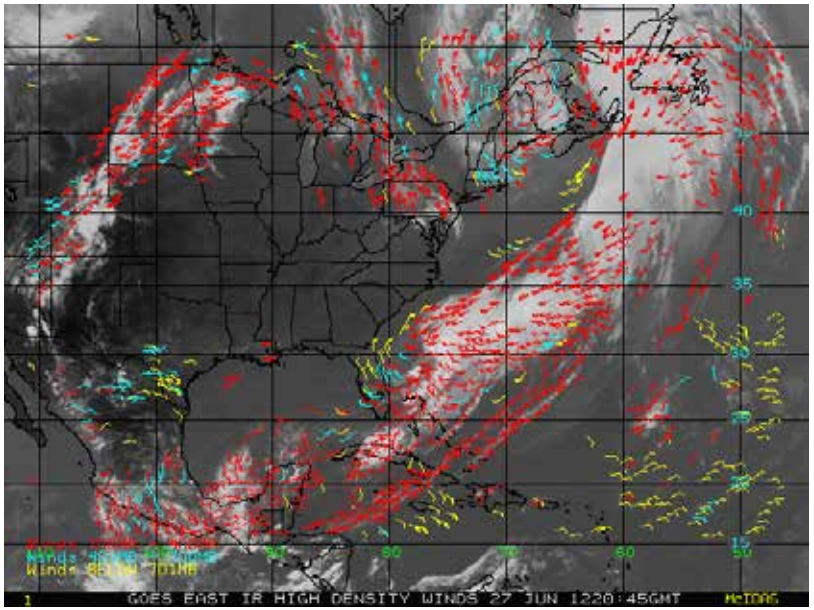

GOES winds derived from cloud and water vapor images (©NOAA)

Venus

Horinouchi et al. (2020)